Journal Section: Development/Plasticity/Repair

Dynamic changes in ultrastructure of the primary cilium in migrating neuroblasts in the postnatal brain

Abbreviated title: Primary cilium in migrating neuroblasts

Mami Matsumoto[1#], Masato Sawada[1#], Diego García-González[2,3], Vicente Herranz-Pérez[4,5], Takashi Ogino[1], Huy Bang Nguyen[6,7], Truc Quynh Thai[6,8], Keishi Narita[9], Natsuko Kumamoto[10], Shinya Ugawa[10], Yumiko Saito[11], Sen Takeda[9], Naoko Kaneko[1], Konstantin Khodosevich[3], Hannah Monyer[2], José Manuel García-Verdugo[4], Nobuhiko Ohno[6,12], Kazunobu Sawamoto[1,13,*]

#Equal contribution

[1] Department of Developmental and Regenerative Neurobiology, Institute of Brain Science, Nagoya City University Graduate School of Medical Sciences, Nagoya 467-8601, Japan.

[2] Department of Clinical Neurobiology, Medical Faculty of Heidelberg University and German Cancer Research Center (DKFZ), 69120 Heidelberg, Germany.

[3] Biotech Research & Innovation Centre, University of Copenhagen, 2200 Copenhagen, Denmark.

[4] Laboratory of Comparative Neurobiology, Cavanilles Institute, University of Valencia, CIBERNED, 46980, Valencia, Spain.

[5] Predepartamental Unit of Medicine, Faculty of Health Sciences, Universitat Jaume I, 12071 Castelló de la Plana, Spain.

[6] Division of Neurobiology and Bioinformatics, National Institute for Physiological Sciences, Okazaki 444-8787, Japan.

[7] Department of Anatomy, Faculty of Medicine, University of Medicine and Pharmacy at Ho Chi Minh City (UMP), Ho Chi Minh city 70000, Vietnam.

[8] Department of Histology-Embryology- Genetics, Factly of Basic Medical Sciences, Pham Ngoc Thach University of Medicine, Ho Chi Minh city 70000, Vietnam.

[9] Department of Anatomy and Cell Biology, Faculty of Medicine, University of Yamanashi, Chuo 409-3898, Japan.
[10] Department of Anatomy and Neuroscience, Nagoya City University Graduate School of Medical Sciences, Nagoya 467-8601, Japan.
[11] Graduate School of Integrated Sciences for Life, Hiroshima University, Hiroshima 739-8521, Japan.
[12] Department of Anatomy, Division of Histology and Cell Biology, Jichi Medical University, School of Medicine, Shimotsuke 329-0498, Japan.
[13] Division of Neural Development and Regeneration, National Institute for Physiological Sciences, Okazaki 444-8585, Japan.

[*]**Correspondence**: Kazunobu Sawamoto, Ph.D.
Department of Developmental and Regenerative Biology, Nagoya City University Graduate School of Medical Sciences
Address: 1 Kawasumi, Mizuho-cho, Mizuho-ku, Nagoya, Aichi 467-8601, Japan
E-mail: sawamoto@med.nagoya-cu.ac.jp
Telephone: +81-52-853-8532 Fax: +81-52-851-1898

Number of Pages: 56
Number of Figures: 8
Number of Table: 1
Number of words: **Abstract** for 229 words; **Introduction** for 647 words; **Discussion** for 1,493 words

Conflict of Interests: The authors declare no competing financial interests.

Acknowledgment We thank J. G. Gleeson, M. Yamaguchi, H. Miyoshi, K. Kaibuchi, T. Seki, S. Ge for materials; H. Oishi, H. Takase, M. Furuse, S. Magi, and K. Kato for technical support; Y. Kato, Y. Hirabayashi, and Sawamoto laboratory members for discussions. This work was supported by research grants from Japan Agency for Medical Research and Development (AMED) (JP19bm0704033 [to K.S.],

JP19gm1210007 [to K.S.], JP19jm0210060 [to M.S., N.K., and K.S.]), Japan Society for the Promotion of Science (JSPS) KAKENHI (26250019, 15H01384, 15H01217, 16H06280, 17H01392, 17H05512, 17H05750, 19H04757, 19H04785, 18KK0213 [to K.S.], 26830014, 18K14823 [to M.S.], 16J00373 [to M.M.]), JSPS Program for Advancing Strategic International Networks to Accelerate the Circulation of Talented Researchers (S2704 [to M.S., V.H-P., N.K., J.M.G-V., and K.S.]), Bilateral Open Partnership Joint Research Projects (to K.S.), Grant-in-Aid for Research at Nagoya City University (to K.S.), Cooperative Study Programs of National Institute for Physiological Sciences [to K.S.], the Mitsubishi Foundation (to K.S.), the Canon Foundation (to K.S.), the Takeda Science Foundation (to K.S. and M.S.), the Spanish Ministry of Science, Innovation and Universities (PCI2018-093062 [to V.H-P., and J.M.G-V.]), and the Independent Research Fund Denmark (8020-00083B [to K.K.]). M.M. was supported by a JSPS Fellowship.

Author contributions M.M., M.S., D.G-G., V.H-P., K.N., N.Ku., S.U., Y.S., S.T., N.Ka, K.K., H.M., J.M.G-V., N.O., and K.S. designed research; M.M., M.S., D.G-G., V.H-P., T.O., H.B.N., T.Q.T., K.K., N.O. performed research; K.N., N.Ku., S.U., Y.S., S.T. contributed unpublished reagents/analytic tools; M.M., M.S., D.G-G., V.H-P., T.O., N.Ku., S.U., N.Ka., K.K., H.M., J.M.G-V., N.O., K.S. analyzed data; M.M., M.S., D.G-G., K.K., K.S. wrote the paper.

Abstract

New neurons, referred to as neuroblasts, are continuously generated in the ventricular-subventricular zone of the brain throughout an animal's life. These neuroblasts are characterized by their unique potential for proliferation, formation of chain-like cell aggregates, and long-distance and high-speed migration through the rostral migratory stream (RMS) toward the olfactory bulb (OB), where they decelerate and differentiate into mature interneurons. The dynamic changes of ultrastructural features in postnatal-born neuroblasts during migration are not yet fully understood. Here we report the presence of a primary cilium, and its ultrastructural morphology and spatiotemporal dynamics, in migrating neuroblasts in the postnatal RMS and OB. The primary cilium was observed in migrating neuroblasts in the postnatal RMS and OB in male and female mice and zebrafish, and a male rhesus monkey. Inhibition of intraflagellar transport molecules in migrating neuroblasts impaired their ciliogenesis and rostral migration toward the OB. Serial section transmission electron microscopy revealed that each migrating neuroblast possesses either a pair of centrioles, or a basal body with an immature or mature primary cilium. Using immunohistochemistry, live imaging, and serial block-face scanning electron microscopy, we demonstrate that the localization and orientation of the primary cilium are altered depending on the mitotic state, saltatory migration, and deceleration of neuroblasts. Together, our results highlight a close mutual relationship between spatiotemporal regulation of the primary cilium and efficient chain migration of neuroblasts in the postnatal brain.

Significance statement

Immature neurons (neuroblasts) generated in the postnatal brain have a mitotic potential and migrate in chain-like cell aggregates toward the olfactory bulb. Here we report that migrating neuroblasts possess a tiny cellular protrusion called a primary cilium. Immunohistochemical studies with zebrafish, mouse, and monkey brains suggest that the presence of the primary cilium in migrating neuroblasts is evolutionarily conserved. Ciliogenesis in migrating neuroblasts in the RMS is suppressed during mitosis and promoted after cell cycle exit. Moreover, live imaging and three-dimensional electron microscopy revealed that ciliary localization and

120 orientation change during saltatory movement of neuroblasts. Our results reveal
121 highly organized dynamics in maturation and positioning of the primary cilium during
122 neuroblast migration that underlie saltatory movement of postnatal-born
123 neuroblasts.

Introduction

The ventricular-subventricular zone (V-SVZ), which lines the lateral walls of the lateral ventricles in the postnatal mammalian brain, harbors neural stem cells (NSCs) that continuously produce immature new neurons (neuroblasts) (Obernier and Alvarez-Buylla, 2019). These neuroblasts are able to divide and migrate in chain-like aggregates toward the olfactory bulb (OB) through the rostral migratory stream (RMS) (Lois and Alvarez-Buylla, 1994; Lois et al., 1996; Luskin, 1993), and toward the lesioned cortex or striatum following brain injury (Arvidsson et al., 2002; Kreuzberg et al., 2010; Parent et al., 2002; Yamashita et al., 2006). Furthermore, the morphology of migrating neuroblasts is highly dynamic and controlled by multiple extrinsic and intrinsic cues (Belvindrah et al., 2011; Fujikake et al., 2018; Khodosevich et al., 2009; Nakamuta et al., 2017; Sawada et al., 2018). However, how ultrastructural features, such as the fine morphology of neurites and the position of internal organelles, contribute to neuroblast migration is not yet fully understood.

The primary cilium is a tiny cellular protrusion that contains signaling receptors on its membrane (Guemez-Gamboa et al., 2014; Malicki and Johnson, 2017), and regulates NSC proliferation (Amador-Arjona et al., 2011; Breunig et al., 2008; Han et al., 2008; Tong et al., 2014) and neuronal maturation (Kumamoto et al., 2012; Luo et al., 2015) in the postnatal brain. Primary cilia are reportedly present in cultured medial ganglionic eminence (MGE)-derived interneurons and cerebellar granule neurons (Baudoin et al., 2012; Trivedi et al., 2014). Both MGE-derived interneurons and V-SVZ-derived neuroblasts show saltatory movement, in which the neuron extends a leading process, forms a swelling, and then translocates its soma toward the swelling (Bellion et al., 2005; Schaar and McConnell, 2005). The primary cilium extends from the basal body (Baudoin et al., 2012), and moves forward into the proximal leading process prior to somal translocation during saltatory movement (Trivedi et al., 2014). Knockout (KO) mice for the ciliary intraflagellar transport (IFT) molecules *Kif3a* or *Ift88*, or the ciliary small GTPase *Arl13b*, showed defective migration, morphogenesis, and connectivity of MGE-derived interneurons (Baudoin et al., 2012; Guo et al., 2017; Higginbotham et al., 2012). *Kif3a* knockdown (KD) also disrupted migration and differentiation of embryonic pyramidal neurons (Chen et al., 2019). However, the

158 primary cilium in postnatal-born neuroblasts migrating in chains in the RMS has not
159 been investigated.
160 Primary cilium ultrastructure and dynamics in mature cells have been
161 intensively studied. Transmission electron microscopy (TEM) analyses have
162 revealed ultrastructural features of the primary cilium, including nine pairs of
163 microtubules (MTs) (the axoneme) and a basal body with transition fibers and basal
164 feet (Sorokin, 1962). Time-lapse imaging studies using fluorescent protein-fused
165 Arl13b have demonstrated the dynamic behavior of the primary cilium (Ford et al.,
166 2018; Higginbotham et al., 2012; Trivedi et al., 2014). In addition to these
167 methodologies, new EM techniques that acquire high-resolution ultrastructural
168 images in three dimensions (3D) have recently been used for primary cilium
169 analysis (Buskin et al., 2018; David et al., 2014; Insinna et al., 2019; Paridaen et al.,
170 2013). Serial block-face scanning electron microscopy (SBF-SEM) is one of the
171 3D-EM techniques that enable analysis of both cell morphology and subcellular
172 organelles simultaneously at the ultrastructure level (Briggman and Bock, 2012;
173 Denk et al., 2012; Ohno et al., 2015). SBF-SEM has been applied to the study of
174 morphological changes in the primary cilium during mitosis in embryonic
175 neuroepithelial cells (Paridaen et al., 2013). Therefore, SBF-SEM may also be
176 useful for studying the morphology of the primary cilium in the V-SVZ-derived
177 neuroblasts migrating in the RMS.
178 In this study, we examined the morphology and dynamics of the primary
179 cilium in V-SVZ-derived neuroblasts migrating in the postnatal RMS and OB. Using
180 time-lapse imaging, TEM, and SBF-SEM, we found that the localization and
181 orientation of the primary cilium in migrating neuroblasts are altered during
182 proliferation and saltatory movement. Our results suggest that the spatiotemporal
183 regulation of the primary cilium is related to the efficient chain migration of
184 postnatal-born neuroblasts.
185

Materials and Methods

Animals

Wild-type (WT) male and female C57BL/6J mice were purchased from Japan SLC (Shizuoka, Japan) (RRID:IMSR_JAX:000664). Male and female *GFP::Centrin2 (GFP::Cent2)* mice (RRID:MGI:3793423) were described previously (Higginbotham et al., 2004), as were male *5HT3A-EGFP* mice (Inta et al., 2008). Male *R26-tdTomato* mice (Stock No. 7914, the Jackson Laboratory; RRID:IMSR_JAX:007914) (Madisen et al., 2010) were provided by Dr. Masahiro Yamaguchi (Kochi Medical School). WT male and female AB (RRID:ZIRC_ZL1) zebrafish (*Danio rerio*) (3–8 months old) were obtained from the Zebrafish International Resource Center, and maintained with standard procedures as reported previously (Kishimoto et al., 2011; Kishimoto et al., 2013; Ogino et al., 2016). The one-year-old male rhesus monkey brain was obtained from EUPRIM-Net biobank (www.euprim-net.eu). All experiments involving live animals were performed in accordance with the guidelines and regulations of Nagoya City University and Heidelberg University.

Viral vectors and plasmids

To generate pENTR-GFP::Centrin2-IRES-Cre, a GFP::Centrin2 fragment was amplified from pEGFP-Cent2 (provided by Dr. Shaoyu Ge, Stony Brook University) by PCR and inserted into the SalI site of pENTR-IRES-Cre (Jinnou et al., 2018; Sawada et al., 2018). To generate pENTR-D-TOPO-dnKif3A, a dnKif3A fragment was amplified from pTetOn-dTomato-F2A-dnKif3A (Kumamoto et al., 2012) by PCR and inserted into the pENTR-D-TOPO vector. Gateway cloning technology (Invitrogen) was used to generate the following expression vectors: CSII-EF-GFP::Centrin2-IRES-Cre, CSII-EF-dnKif3A-IRES-Venus, and pCAGGS-dnKif3A. To generate CSII-CMV-Arl13b::Venus, an Arl13b::Venus fragment was inserted into the Eco47III site of CSII-CMV-MCS-IRES2-Bsd. CSII lentiviral vectors were provided by Dr. Hiroyuki Miyoshi (RIKEN Tsukuba BioResource Center). To generate lentiviral particles, lentiviral vectors and packaging vectors (pCAG-HIVgp and pCMV-VSV-G-RSV-Rev) were transfected into HEK293T cells. Three days after transfection, the culture supernatants were

concentrated by centrifuging at 8,000 rpm at 4ºC for 16 h using an MX-307 refrigerated microcentrifuge (Tomy).

To obtain pCDH-CMV-5HT6::GFP and pCDH-CMV-ACIII::GFP lentiviral vectors, 5HT6::GFP (Addgene #35624) and ACIII::GFP (kindly provided by Dr. Joshua J. Breunig) (Guadiana et al., 2013) cassettes were subcloned into the lentiviral vector pCDH-CMV (the original pCDH plasmid was from System Bioscience). Recombinant viruses were produced and titrated as before (Khodosevich et al., 2013; Khodosevich et al., 2012). Briefly, HEK293 cells were transfected with the viral backbone vector together with lentiviral helper plasmids (pMDLgpRRE, pRSV-Rev and pMD2.G), and viral particles were collected by ultracentrifugation (~120,000 g; Beckman) 48–60 h post-transfection. The viral pellet was resuspended in D-phosphate buffered saline (PBS), aliquoted, and stored at -80ºC until use. Viral titers were determined by infecting HEK293 cells in 96-well plates across 5 orders of dilutions. Before injection, viral titer was adjusted to $2 \times 10^7 – 2 \times 10^8$ fluorescent plaque-forming units (fpfu)/mL.

For an IFT88-KD experiment using retrovirus, pU6-shRNA IFT88-EF1a-EGFP (provided by Dr. Shaoyu Ge, Stony Brook University) was used as reported previously (Kumamoto et al., 2012). To generate retroviral particles, pU6-shRNA IFT88-EF1a-EGFP and packaging vectors (pCAG-HIVgp and pCMV-VSV-G-RSV-Rev) were transfected into HEK293gp cells. Three days after transfection, the culture supernatants were concentrated by centrifugation as descrived above. To visualize 5HT3A localization in migrating neuroblasts, a retrovirus expressing 5HT3A::GFP (MMLV-RSV-EGFP-5HT3A) was used as reported previously (Garcia-Gonzalez et al., 2017). Recombinant retroviruses were produced by transfection of HEK293 cells with retroviral vectors and helper plasmids (pGP and pMD2.G), and viral particles were collected by ultracentrifugation as described above. The viral pellet was resuspended in D-PBS and viral titer was adjusted to $2 \times 10^7 – 2 \times 10^8$ fpfu/mL before injection.

To generate pEGFP-N1-SSTR3::GFP, an SSTR3::GFP fragment was inserted into the HindIII/KpnI sites of pEGFP-N1 (Clontech). To generate pdTomato-C1-Cent2 (dTomato::Cent2), EGFP cDNA in pEGFP-Cent2 (Kumamoto et al., 2012) was replaced with dTomato cDNA. pcDNA3.1-EB3-mEGFP (EB3::GFP) was provided by Dr. Kozo Kaibuchi (Nagoya University) (Watanabe et al., 2015).

In vivo viral infection and transplantation

Injection of lentiviral suspension into the V-SVZ of adult WT and *R26-tdTomato* mice was performed as described previously (Sawamoto et al., 2006) with modification. A 2-μL volume of lentiviral suspension was stereotaxically injected into the anterior V-SVZ (1.0 mm anterior, 1.0, 1.1, 1.2 mm lateral to bregma and 1.8–2.3 mm deep) of male adult WT and *R26-tdTomato* mice. For injection of retrovirus encoding Ift88 shRNA, 2 μL of retroviral suspension was stereotaxically injected into the anterior V-SVZ (1.0 mm anterior, 1.0, 1.1, 1.2 mm lateral to bregma and 1.8–2.3 mm deep) of male adult WT mice. For injection of retrovirus expressing 5HT3A::GFP, 1 μL of retroviral suspension was stereotaxically injected into the anterior V-SVZ (0.6 mm anterior, 1.2 mm lateral to bregma and 1.7 mm deep) of P20 male WT mice, as reported previously (Garcia-Gonzalez et al., 2017).

Transplantation of neonatal V-SVZ cells into the V-SVZ of adult WT mice was performed as described previously (Sawada et al., 2018) with modification. The V-SVZ tissues from postnatal day 0–1 (P0–1) WT mice were dissected and dissociated with trypsin-EDTA (Invitrogen). The cells were washed with L-15 medium (Invitrogen) containing 40 μg/ml DNase I (Roche) and transfected with 2.0 μg pEGFP-N1-SSTR3::GFP using the Amaxa Nucleofector II system (Lonza). The transfected cells were resuspended in L-15 medium and stereotaxically injected into the anterior V-SVZ (1.0 mm anterior, 1.0, 1.1, 1.2 mm lateral to bregma and 1.8-2.3 mm deep) of adult male WT mice.

In vitro time-lapse imaging of migrating neuroblasts

In vitro culture of V-SVZ-derived neuroblasts was performed as described previously (Ota et al., 2014; Sawada et al., 2018). The V-SVZ tissues were dissected from P0–1 male and female WT mice and dissociated with trypsin-EDTA (Invitrogen). The cells were washed in L-15 medium (Invitrogen) containing 40 μg/mL DNase I (Roche) and transfected with plasmids using the Amaxa Nucleofector II system (Lonza). The transfected cells were recovered in RPMI-1640 medium (Thermo Fisher Scientific), allowed to aggregate, and then embedded in 60% Matrigel (BD Biosciences) in L-15 medium. The cell aggregates were cultured in Neurobasal medium containing 2% NeuroBrew-21 (Invitrogen), 2 mM L-glutamine (Gibco), and 50 U/mL penicillin-streptomycin (Gibco) for 2 days.

Four-dimensional time-lapse images of the basal body and primary cilium in migrating neuroblasts were captured at 2-min and 0.6-μm intervals using an LSM880 laser-scanning confocal microscope (Carl Zeiss) and a 63× oil-immersion objective lens. Time-lapse images of DsRed-expressing migrating neuroblasts in chains were captured at 1-min intervals using an inverted light microscope (Axio-Observer, Carl Zeiss) equipped with a Colibri light-emitting diode light system and a 40× objective lens, as reported previously (Sawada et al., 2018). Behaviors of migrating neuroblasts and GFP::Cent2+ basal body were tracked using the ImageJ manual tracking tool. The resting phase was defined as a migration speed less than 12 μm/h (Jinnou et al., 2018). Three-dimensional reconstructions of migrating neuroblasts were performed using Imaris (Carl Zeiss) as reported previously (Hikita et al., 2014), based on the faint cytosolic GFP+ (Fig. 2B) or dTomato+ (Fig. 2G) signals.

For EB3::GFP imaging, time-lapse images of EB3::GFP+ dots in migrating neuroblasts were captured at 4-s intervals using an LSM880 laser-scanning confocal microscope (Carl Zeiss) and a 63× oil-immersion objective lens, as reported previously (Sawada et al., 2018) with modification. All the EB3::GFP+ dots pursuable for 8 s (three sequential frames) were tracked using the ImageJ manual tracking tool, and their moving speed was measured using the ImageJ manual tracking tool.

Immunohistochemistry and image acquisition

Immunohistochemistry in mouse brain sections was performed as described previously (Ota et al., 2014; Sawada et al., 2018). Briefly, the adult brains were fixed by transcardiac perfusion with 4% paraformaldehyde (PFA) in 0.1 M phosphate buffer (PB), and postfixed overnight at 4ºC in the same fixative. Fifty-micrometer-thick floating coronal and sagittal sections were made using a vibratome (VT-1200S, Leica), and incubated for 30 min at room temperature (RT) in 10% normal donkey serum (NDS) and 0.2% Triton X-100 in PBS (blocking solution). These sections were incubated with primary antibodies in blocking solution overnight at 4ºC, and with AlexaFluor488/568/647-conjugated secondary antibodies (1:1,000, Invitrogen) for 2 h at RT in blocking solution. The following primary antibodies were used: rabbit anti-adenylate cyclase III (ACIII) (1:200, sc-588, Santa Cruz Biotechnology; RRID:AB_630839); mouse IgG anti-Arl13b (1:1,000, 75-287,

NeuroMab; RRID:AB_2341543); rabbit anti-doublecortin (Dcx) (1:1,000, 4604S, Cell Signaling Technology; RRID:AB_10693771); rabbit anti-DsRed (1:1,000, 632496, Clontech; RRID:AB_10013483); rabbit anti-GFP antibody (1:1,000, A6455, Invitrogen; RRID:AB_221570); rat anti-GFP (1: 1000, 04404-84, Nacalai Tesque; RRID:AB_10013361); rabbit anti-calbindin (CB) (1:1,000, CB38, Swant; RRID:AB_2721225); rabbit anti-calretinin (CR) (1:1,000, 7697, Swant; RRID:AB_2619170); rabbit anti-Ki67 (1:1,000, Leica Biosystems, NCL-Ki67p; RRID:AB_442102); rabbit anti-parvalbumin (PV) (1:1,000, PV235, Swant; RRID:AB_10000343); mouse IgG anti-phospho-histone H3 (pHH3) (1:1,000, 9706, Cell Signaling Technology; RRID:AB_331748); sheep anti-tyrosine hydroxylase (TH) (1:1,000, AB1542, Millipore; RRID:AB_11213126) antibodies. Nuclei were stained with Hoechst 33342 (1:5,000, Invitrogen).

Immunohistochemistry in zebrafish brain sections was performed as described previously (Kishimoto et al., 2011; Ogino et al., 2016). The fish were anesthetized with tricaine. The brain was dissected and fixed with 4% PFA in 0.1 M PB overnight at 4ºC. Fifty-micrometer-thick floating coronal sections were made using a vibratome (VT-1200S, Leica), and incubated for 30 min at RT in 10% NDS and 0.2% Triton X-100 in PBS (blocking solution). These sections were incubated with primary antibodies in blocking solution overnight at 4ºC, and with AlexaFluor488/568-conjugated secondary antibodies (1:500, Invitrogen) for 2 h at RT in blocking solution. The following primary antibodies were used: mouse IgM anti-polysialylated form of neural cell adhesion molecule (PSA-NCAM) (1:1,000, a kind gift from Dr. Tatsunori Seki, Tokyo Medical University) (Seki and Arai, 1991); mouse IgG anti-acetylated tubulin (1:1,1000, Sigma; RRID:AB_477585). Nuclei were stained with Hoechst 33342 (1:5,000, Invitrogen).

Immunohistochemistry in rhesus monkey brain sections was performed as described previously (Garcia-Gonzalez et al., 2017). Briefly, the brain was dissected, fixed with 4% PFA in 0.1 M PB 24 h at 4ºC, and cut into 0.5 cm slabs. These slabs were postfixed with 4% PFA in 0.1M PB, cryoprotected with 30% sucrose for 72 h. Fifty-micrometer-thick coronal sections were prepared by cryostat (Leica Biosystems). These sections were incubated for 30 min at RT with 5% bovine serum albumin and 0.5% Triton X-100 in blocking solution, primary antibodies in blocking solution for 48 h at 4ºC, and AlexaFluor488/568-conjugated secondary antibodies in blocking solution for 24 h at 4ºC. The following primary

355 antibodies were used: goat anti-Dcx antibody (1:250, sc-8066, Santa Cruz
356 Biotechnology; RRID:AB_2088494); mouse IgG anti-Arl13b (1:1,000, 75-287,
357 NeuroMab; RRID:AB_2341543). Nuclei were stained with DAPI (1:5,000, Thermo
358 Fisher Scientific; RRID:AB_2307445).
359 Images of stained RMS and OB sections were acquired by scanning at
360 0.4-μm (Fig. 1, 3C, F) or 2-μm (Fig. 3A, B, D, E, G–I) intervals using an LSM 700
361 confocal laser-scanning microscope (Carl Zeiss) with a 40× water-immersion
362 objective lens. To investigate the positional relationship of the basal body and
363 primary cilium in detail (Fig. 1B), images of GFP::Cent2+ signals and Arl13b+
364 signals were acquired by scanning at 0.4-μm intervals using an LSM 880 Airyscan
365 confocal laser-scanning microscope with a 63× oil-immersion objective lens. For
366 quantification of labeled cells in viral experiments (Fig. 3), all the labeled cells
367 observed in the RMS and OB in every section (dnKif3A) or every third section
368 (IFT88-KD) were counted.
369
370 **Transmission electron microscopy**
371 Sample preparation for TEM was performed as described previously
372 (Kaneko et al., 2018). Adult male mouse brains were fixed by transcardiac perfusion
373 with 2% PFA and 2.5% glutaraldehyde (GA) in 0.1 M PB (pH 7.4) at 4ºC, and
374 postfixed overnight at 4ºC in the same fixative. These brains were cut into
375 200-μm-thick coronal sections using a vibratome (VT-1200S, Leica) (anterior +2.0–
376 2.3 mm from bregma). The sections were treated with 2% Osmium tetroxide (OsO_4,
377 Electron Microscopy Sciences) in 0.1 M PB (pH 7.4) at 4ºC, dehydrated with a
378 graded series of ethanol, placed in propyleneoxide (Nissin EM), and embedded in
379 Durcupan resin for 72 h at 60°C. Semi-thin sections (1.5-μm-thick) were
380 sequentially cut using an ultramicrotome (UC6, Leica) with a diamond knife (histo,
381 DiATOME), and stained with 1% toluidine blue, and sections of interest were
382 chosen under a light microscope CX23 (Olympus). Ultra-thin sections (60–
383 70-nm-thick) were sequentially cut from the embedded semi-thin sections using an
384 ultramicrotome (UC6, Leica) with a diamond knife (SYM2045, SYNTEK), and
385 stained with 2% uranyl acetate in distilled water for 15 min and with modified Sato's
386 lead solution for 5 min. TEM images of the primary cilium in neuroblasts were
387 acquired using a JEM-1400plus (JEOL) fitted with a digital camera. Thirty-six
388 neuroblasts were examined in this study.

Serial block-face scanning electron microscopy (SBF-SEM)

Sample preparation, observation with SBF-SEM and analyses of acquired data were performed as described previously with slight modifications (Kaneko et al., 2018; Nguyen et al., 2016; Sawada et al., 2018; Thai et al., 2016). Adult WT brains were fixed by transcardiac perfusion with 2.5% GA and 2% PFA in 0.1 M PB (pH 7.4) at 4ºC, and postfixed overnight at 4ºC in the same fixative. Fixed RMS tissues (anterior +2.0–2.3 mm from bregma) were treated with 2% OsO_4 and 1.5% potassium hexacyanoferrate in PBS for 1 h at 4ºC, 1% thiocarbohydrazine for 20 min at RT, 2% aqueous OsO_4 for 30 min at RT, and lead aspartate solution for 30 min at 65ºC. The RMS tissues were then dehydrated in a graded ethanol series, treated with dehydrated acetone, and embedded in Quetol 812 epoxy resin containing Ketjen black powder for 3 h at 95ºC to ensure polymerization. SBF-SEM observation of the RMS and OB was performed using a Merlin and Sigma scanning electron microscope (Carl Zeiss) equipped with a 3View in-chamber ultramicrotome system (Gatan). Serial image sequences were 40.96 × 40.96 μm wide (5.0 nm/pixel) and > 80 μm deep with 80-nm steps. Sequential images were processed using FIJI. In the image stacks, about 2% of the total images were replaced by neighboring images because some parts of the images were contaminated by debris or corrupted during image acquisition. Our SBF-SEM analyses contained neuroblasts with whole and partial morphology (“whole cells” and “partial cells”, respectively). “Partial cells”, containing part of the nucleus, Golgi apparatus, and centrosome or basal body with ciliary structures, and having a leading process longer than 6 μm, were used for analyses of neuroblast orientation in the RMS (described in the Results section), ciliary classification (Fig. 7A), and ciliary length (Fig. 7C). Numbers of analyzed whole and partial cells in the SBF-SEM analyses (Figs. 5–7) are summarized in Table 1. Segmentation of the cell membrane, nuclei, centrioles, mitochondria, Golgi apparatus, and primary cilium were performed using Microscopy Image Browser (Belevich et al., 2016). Manual segmentation was done in every 2nd–10th and interpolation tool was used for the other slices. Three-dimensional reconstruction of migratory neuroblasts and their subcellular organs was performed using Amira software (Maxnet) as reported previously (Kaneko et al., 2018; Sawada et al., 2018). Three-dimensional object files (.obj) obtained from Amira software were further processed by Blender software

(https://www.blender.org/), and visualized as interactive 3D models by Sketchfab (https://sketchfab.com).

Experimental design and statistical analysis

Statistical analyses were performed using EZR (Kanda, 2013), as reported previously (Fujikake et al., 2018). The experiments were not randomized. Sample sizes were not predetermined, but were chosen based on previous studies. All the numerical data except for Fig. 7M were two-sided, and are shown as the mean ± SEM. The normality of the data was analyzed by Kolmogorov-Smirnov test. For normally distributed data, equality of variances was examined by *F*-test, and a comparison of means between two independent groups was carried out by unpaired *t*-test or Welch's *t*-test. For comparisons of means among three or more independent groups, one-way ANOVA followed by Tukey-Kramer test was applied. To analyze the data set from multiple observations of individual samples, two-way repeated-measures ANOVA followed by *post-hoc* Tukey-Kramer test or unpaired *t*-test between groups with Bonferroni correction was performed. For not normally distributed data, a comparison of medians between groups was carried out by Mann-Whitney *U*-test, Kruskal-Wallis test followed by Steel-Dwass test, or Friedman's test followed by Wilcoxon signed rank test with Bonferroni correction. In Fig. 7M, all the data indicate the probability, and they were compared by Fisher's exact test. A *p*-value less than 0.05 was considered to be statistically significant.

Results

Expression of ciliary markers in migrating neuroblasts in the postnatal vertebrate RMS

To examine whether migrating neuroblasts in the postnatal RMS and OB present a primary cilium, we first stained brain sections for primary cilium marker Arl13b (Caspary et al., 2007) (Fig. 1A1–B'). To observe the basal body and a ciliary marker simultaneously, we studied doublecortin-positive (Dcx+) neuroblasts in transgenic mice expressing GFP-tagged Centrin-2 protein (GFP::Cent2) (Fig. 1A1–A2') or V-SVZ-derived neuroblasts in WT mice infected with the GFP::Cent2-expressing lentivirus (Fig. 1B, B') (Higginbotham et al., 2004; Kumamoto et al., 2012). An Arl13b-positive (Arl13b+) structure was observed in close proximity to one of the centrioles in the Dcx+ neuroblasts in the RMS and OB, suggesting that it is associated with the basal body. Another marker for the primary cilium, adenylate cyclase III (ACIII) (Bishop et al., 2007), is reported to be expressed in mature granule cells in the OB (Luo et al., 2015). ACIII was also detectable in migrating neuroblasts in the RMS (Fig. 1C) and mature interneurons in the external plexiform layer and glomerular layer of the OB (Fig. 1D–G). Moreover, fluorescent protein-tagged ciliary markers such as Arl13b::Venus (Fig. 1H), ACIII::GFP (Fig. 1I), and 5HT6::GFP (Fig. 1J) (Brailov et al., 2000) accumulated in the perinuclear region of Dcx+ neuroblasts in the RMS. These results suggest that the migrating neuroblasts possess a primary cilium in the postnatal RMS and OB.

A functional primary cilium expresses signaling receptors on its membrane (Malicki and Johnson, 2017; Wheway et al., 2018). To investigate the subcellular localization of ciliary receptors in migrating neuroblasts in the RMS, we introduced GFP-tagged serotonin receptor 3A (5HT3A::GFP) or somatostatin receptor-3 (SSTR3::GFP) into migrating neuroblasts. These ciliary receptors colocalized with a ciliary marker (ACIII or Arl13b) (Fig. 1K–M'), suggesting that V-SVZ-derived migrating neuroblasts possess a functional primary cilium in the postnatal RMS.

Furthermore, we examined whether the expression of ciliary markers in migrating neuroblasts in the RMS is conserved in other vertebrates. We observed an acetylated tubulin-positive primary cilium in neuroblasts in the adult zebrafish RMS (Fig. 1N, N'), and an Arl13b-positive primary cilium in the one-year-old rhesus monkey RMS and OB (Fig. 1O–P''). Collectively, these results suggest that the

V-SVZ-derived migrating neuroblasts possess a primary cilium in the postnatal vertebrate brain.

Dynamic changes in primary cilium localization during neuronal saltatory migration

Previous EM studies have shown that the primary cilium is located at the cell surface at a distance from the nucleus, or in the perinuclear cytosol, in cultured MGE-derived interneurons (Baudoin et al., 2012). Furthermore, time-lapse imaging of Arl13b::Venus in cultured cerebellar granule neurons revealed that the primary cilium dynamically moves with the basal body (Trivedi et al., 2014). To study the subcellular localization of the primary cilium during saltatory movement in chain-forming neuroblasts, Arl13b::Venus was introduced into V-SVZ cells dissected from P0–1 *GFP::Cent2* mice (Fig. 2A). Saltatory movement of neuroblasts was divided into three phases: leading-process extension phase, swelling-formation phase, and somal translocation phase, as reported previously (Sawada et al., 2018). Three-dimensional confocal time-lapse imaging revealed that the primary cilium is submerged in the cytosol or extended from the cell surface (Fig. 2B–E'). The proportion of primary cilium extension from the cell surface was significantly higher in swelling-formation phase than in other phases (Fig. 2C–F), suggesting that the extension of the primary cilium is promoted transiently prior to somal translocation in cultured chain-forming neuroblasts.

During neuronal deceleration in the postnatal OB, V-SVZ-derived neuroblasts transiently form a filopodium-like lateral protrusion (FLP) from the proximal leading process in the swelling-formation phase, which coincides with the pausing of somal translocation (Sawada et al., 2018). We found that both chain-forming and FLP-bearing neuroblasts extend a primary cilium from the cell surface during the swelling-formation phase (Fig. 2B–E', G–J'). The basal body with extended primary cilium was observed to be continuously migrating forward during the swelling-formation phase in chain-forming neuroblasts (Fig. 2B, 10–14 min), but not in FLP-bearing ones (Fig. 2G), suggesting that FLP formation is related to the migration termination of the primary cilium in the leading process.

Together, these results suggest that the primary cilium localization changes spatiotemporally during saltatory movement in cultured V-SVZ-derived migrating neuroblasts.

Inhibition of Kif3A and IFT88 impairs ciliogenesis and saltatory movement of V-SVZ-derived neuroblasts

The IFT molecules Kif3A and IFT88 control formation of the primary cilium and migration of pyramidal neurons (Chen et al., 2019) and interneurons (Baudoin et al., 2012) in the embryonic cerebral cortex. Loss-of-function of *Kif3a* or *Ift88* causes impaired ciliogenesis, leading process morphology, and centrosomal movement in the MGE-derived cortical interneurons, leading to their abnormal directionality during migration and altered final distribution in the cerebral cortex (Baudoin et al., 2012). To examine the effects of Kif3A inhibition on V-SVZ-derived neuroblasts in the RMS, we injected a lentivirus expressing a dominant-negative form of Kif3A (dnKif3A) and Venus into the V-SVZ of adult WT mice. At 7 days post-injection (dpi), the proportion of neuroblasts with an Arl13b+ primary cilium (Fig. 3A–C) and of those that had reached the OB (Fig. 3D) was decreased by dnKif3A expression, suggesting that ciliogenesis and migration toward the OB were disturbed. Unlike the deformation of leading process reported in Kif3A-deficient MGE-derived interneurons (Baudoin et al., 2012), the morphology of dnKif3A-expressing chain-forming neuroblasts was indistinguishable from the control (Fig. 3A, B). In the RMS, the proportion of neuroblasts pointing toward the OB was significantly decreased by dnKif3A expression (Fig. 3E). Similar defects in ciliogenesis and rostral migration in the V-SVZ-derived neuroblasts were also observed by IFT88-KD (Fig. 3F–H). At 14 dpi, a significantly larger proportion of V-SVZ-derived neuroblasts was observed to remain in the RMS in the dnKif3A-expressing group compared with the control (Fig. 3I). Thus, loss-of-function of IFT molecules disrupted primary cilium formation and rostral migration in V-SVZ-derived neuroblasts in the RMS.

To study the effect of dnKif3A expression on neuronal saltatory movement in greater detail, we analyzed the migratory behavior of dnKif3A-expressing cultured neuroblasts dissected from the V-SVZ of P0–1 *GFP::Cent2* mice (Fig. 3J–V, Movie 1). The dnKif3A-expressing neuroblasts spent longer in both the resting and migratory phases, and showed a decreased migration speed (Fig. 3J–N). In the resting phase, while dnKif3A expression did not affect leading process extension (Fig. 3O, P), it slowed basal body speed (Fig. 3Q) without affecting its stride (Fig. 3R). Moreover, dnKif3A expression increased the frequency of backward basal

body migration in the leading process (Fig. 3K, 0-24 min; Fig. 3S). In the migratory phase, dnKif3A expression decreased somal speed (Fig. 3T) but not stride (Fig. 3U). dnKif3A expression increased the frequency of reversal turn of neuroblasts (Fig. 3K, 24–54 min; Fig. 3V). Similar to MGE-derived interneurons (Baudoin et al., 2012), the phenotypes caused by the inhibition of IFT molecules suggest that the basal body and the primary cilium are involved in the saltatory migration of V-SVZ-derived neuroblasts.

Fine morphology of the primary cilium in migrating neuroblasts in the postnatal RMS

We investigated the ultrastructure of the primary cilium in migrating neuroblasts in the adult RMS using serial-section TEM (36 cells from five mice). Immature neuroblasts with migratory features in the RMS were identified based on their electron-dense nucleus with multiple nucleoli, dark cytoplasm with many free ribosomes, and the presence of extracellular spaces between neuroblasts, as described previously (Doetsch et al., 1997). Serial TEM images of migratory neuroblasts in the RMS showed either a pair of centrioles (Fig. 4A, 5/36 cells), or a basal body with an immature or mature primary cilium (Fig. 4B–E', 31/36 cells). MTs were radially extended from the basal body of the primary cilium (Fig. 4D, z = 1 and 2), suggesting that the basal body acts as a microtubule-organizing center (MTOC) in migrating neuroblasts. The immature or mature primary cilium attached to the basal body (31 cells) was further classified into four types: ciliary vesicle, procilium, non-extended primary cilium, and extended primary cilium (Fig. 4B–E, see below).

In previous studies on primary cilium development in immature neurons, two types of immature forms of the primary cilium have been described: ciliary vesicles (Baudoin et al., 2012) and procilium (Arellano et al., 2012). Ciliary vesicles are attached to the basal body in the cytosol (Baudoin et al., 2012). The procilium is a membrane protrusion from the plasma membrane containing no axonemal structures (Arellano et al., 2012). We found immature primary cilia similar to ciliary vesicles (Fig. 4B, 6/31 cells) and to the procilium (Fig. 4C, 4/31 cells) in migratory neuroblasts in the RMS. In addition, elongated ciliary structures with a 9+0 ciliary axoneme and a ciliary pocket, a typical morphology of the mature primary cilium (Sorokin, 1962), were observed in migratory neuroblasts in the RMS (Fig. 4D–F, 21/31 cells). The tip of the primary cilium of these cells (21 cells) was observed to

be either non-extended (Fig. 4D, D', 18 cells) or extended (Fig. 4E, E', 3 cells) from the cell surface, which we defined as a "non-extended primary cilium" and an "extended primary cilium", respectively. Interestingly, the tip of the non-extended primary cilium appeared to have access to the extracellular environment even under its submerged state (Fig. 4D', yellow arrows). Collectively, these observations suggest that the primary cilium of immature migratory neuroblasts showed diverse morphologies in the postnatal RMS.

Three-dimensional ultrastructural features of migrating neuroblasts in the postnatal RMS analyzed by serial block-face scanning electron microscopy

SBF-SEM is a powerful tool to study both whole cell morphology and its subcellular organs at an ultrastructural level (Briggman and Bock, 2012; Denk et al., 2012; Ohno et al., 2015). Since chain-forming neuroblasts align along the rostrocaudal axis in the anterior RMS, repeated coronal sectioning and image acquisition of RMS tissues by SBF-SEM efficiently include migrating neuroblasts. To establish criteria for cell-type identification, ultrastructural features of adult mouse RMS cells observed under SBF-SEM (Fig. 5, 6; Movie 2) were compared with those observed under TEM, which have been reported previously (Doetsch et al., 1997).

Immature migratory neuroblasts could be identified in the SBF-SEM images by a smooth cell contour, dark cytoplasm with small Golgi apparatus and a few short endoplasmic-reticulum fragments, and the presence of extracellular spaces, similar to the TEM images, as we reported previously (Kaneko et al., 2018; Sawada et al., 2018) (Fig. 5A). While the TEM images clearly showed adherens junction (AJ)-like structures and an MT network in migratory neuroblasts (Doetsch et al., 1997; Fujikake et al., 2018; Sawada et al., 2018), our SBF-SEM images could not clearly visualize these structures. By performing 3D reconstruction of neuroblasts in the RMS, we examined 330 cells with whole morphology and 88 cells with partial morphology, which lack part of the leading process and/or soma (for a detailed definition of "partial cells", see Materials and Methods). The majority of identified neuroblasts were oriented rostrally (87.1 ± 1.4%, 292/330 whole cells and 72/88 partial cells from five mice) and tightly attached to their neighboring neuroblasts, forming chains in the RMS (Fig. 5A).

In addition to migratory neuroblasts, tunnel-forming astrocytes, oligodendrocytes, and microglia were observed in and around the RMS. Tunnel-forming astrocytes were identified by an irregular contour, light cytoplasm with long endoplasmic reticulum, and abundant intermediate filaments (Fig. 5B–B''), similar to the TEM images that have been reported previously (Doetsch et al., 1997). These astrocytes enwrapped the blood vessels and/or neuronal chains by their processes to form a glial tube in the RMS. Oligodendrocytes were located around the RMS and could be identified by a smooth and round contour, short and dilated endoplasmic reticulum, and direct contacts with myelinated and non-myelinated axons (Fig. 5C, C') (Menn et al., 2006). Microglia were identified by an irregular contour with elongated processes, dark cytoplasm with long endoplasmic reticulum and lysosomes, and the presence of extracellular spaces (Fig. 5D, D') (Capilla-Gonzalez et al., 2014). Thus, SBF-SEM successfully classified all major cell types in the postnatal RMS based on their ultrastructural features.

We next compared the SBF-SEM images of neuroblasts with the time-lapse images of cultured chain-forming neuroblasts during saltatory movement (Fig. 5E–H). The tip of the leading process showed a spread growth-cone-like structure during leading-process extension and swelling-formation phases (Fig. 5E, black arrowheads) that collapsed during somal translocation phase (Fig. 5E, white arrowhead). Swelling was observed after the extension of the leading process and before the ending of somal translocation, as reported previously (Ota et al., 2014; Sawada et al., 2018) (Fig. 5E, arrows). Consistent with these findings, three-dimensional reconstruction of cell contour based on the SBF-SEM images visualized a long leading process, with or without swelling, which has a spread or collapsed growth cone at its tip, in addition to an elongated cell body and trailing process (Fig. 5F–H, Movie 3–6). Thus, by analyzing the morphology of the swelling and growth cone, we could identify the migration phase of each neuroblast in SBF-SEM images.

Three-dimensional reconstruction also revealed that mitochondria and the Golgi apparatus were mainly distributed in the proximal leading process or swelling, as reported previously (Bellion et al., 2005; Lin-Hendel et al., 2016) (Fig. 5F–H). While there was no significant difference in the numbers of mitochondria in neuroblasts that showed leading process extension, swelling formation, and somal translocation, their distribution was altered depending on saltatory movement

(Lin-Hendel et al., 2016) (Fig. 5F–H, magenta, Fig. 5I). Mitochondria located in the proximal leading process were longer than those in the distal leading process (Fig. 5J, K; distal leading process, 0.58 ± 0.02 μm [n = 166 from 18 cells]; proximal leading process, 1.04 ± 0.03 μm [n = 417 from 18 cells]; W = 19594, $p = 2.6 \times 10^{-16}$, Mann-Whitney U-test). Taken together, these findings suggest that mitochondria and the Golgi apparatus move in a saltatory movement-dependent manner in migratory neuroblasts *in vivo*.

In contrast to immature neurons migrating in the developing brain, V-SVZ-derived neuroblasts have remarkable mitotic potential during their migration in the RMS (Ikeda et al., 2010; Ponti et al., 2013). To examine the relationship between mitotic states and ciliogenesis in migrating neuroblasts in the RMS, we classified Dcx+ cells into proliferating or non-proliferating neuroblasts based on expression of the cell cycle marker Ki67. Proliferating neuroblasts were further divided into two subgroups: M phase (with a mitotic nucleus) or G1/S/G2 phases (Fig. 5L–N). In proliferating neuroblasts, an Arl13b+ primary cilium was observed less frequently and its length was shorter, compared with these features in non-proliferating neuroblasts (Fig. 5O). Among these proliferating neuroblasts, the proportion of cilium-bearing neuroblasts was lower in M phase than in G1/S/G2 phases (Fig. 5O), suggesting that ciliogenesis is transiently suppressed during mitosis. In the SBF-SEM analysis, dividing neuroblasts in the adult RMS possessed two pairs of centrioles, divided nuclei, no apparent Golgi apparatus (Danilov et al., 2009), and no primary cilium (Fig. 5P–Q, Movie 7). Taken together, these results suggest that mitotic states affect ciliogenesis in migrating neuroblasts in the postnatal RMS.

Changes in subcellular localization and orientation of the primary cilium during saltatory movement of migrating neuroblasts in the postnatal brain

To visualize the fine whole-cell morphology of migrating neuroblasts in the adult RMS and primary cilium *in vivo*, we reconstructed their images three-dimensionally (Fig. 6, 7; 330 whole cells from five mice). Consequently, a pair of centrioles (Fig. 6A–B', Movie 8) or one of four types of primary cilium (Fig. 6C–J', Movie 9–12) was observed adjacent to the Golgi apparatus (100 ± 0%, 330 whole cells from five mice) in migratory neuroblasts.

In the adult RMS, a mature primary cilium was observed in 59.8 ± 3.3% of migratory neuroblasts, most of which (81.8 ± 1.7%) were classified as the non-extended type (Fig. 7A). The remaining 40.2 ± 3.3% had centrioles, ciliary vesicles, or a procilium (Fig. 7A). Consistent with the results of live imaging of cultured neuroblasts (Fig. 2A–F), the proportions of extended primary cilium and procilium were larger in the swelling-formation phase than in other phases of saltatory movement (Fig. 7B). The primary cilium length was not significantly different between non-extended and extended forms in the RMS (Fig. 7C). These results suggest that extension of the mature and immature primary cilium is promoted transiently during the swelling-formation phase of saltatory movement in chain-forming migrating neuroblasts *in vivo*.

While immature neuroblasts migrate in chains at a high speed in the RMS, these neuroblasts detach from chains to migrate individually, and transiently form FLPs during migration termination in the OB (Sawada et al., 2018). In contrast to the chain-forming neuroblasts in the RMS, those in the granule cell layer of the OB, which are radially dispersed and have an elongated leading process, could not be included in our imaging volume (40 × 40 × 80 μm). Therefore, we analyzed 25 partial OB cells from three mice. We investigated the primary cilium morphology in immature neuroblasts in the OB, and found a mature primary cilium in 84.9 ± 11.4% of these neuroblasts (Fig. 7A). The proportion of extended primary cilium was significantly larger in FLP-bearing neuroblasts than in neuroblasts without FLP (Fig. 6K, K'; FLP-bearing neuroblasts, 95.2 ± 4.8%; neuroblasts without FLP, 22.2 ± 14.7%; $t_{(4)}$ = -4.73, p = 0.0091, paired t-test; n = 3 mice). Furthermore, the extended primary cilium was longer than the non-extended primary cilium in the OB, and both were longer than their counterparts in the RMS (Fig. 7C). Together, these results suggest that the elongation and extension of primary cilium are promoted in individual decelerating neuroblasts in the OB.

To understand the extracellular microenvironment of the extended primary cilium in migrating neuroblasts in the RMS and OB, we identified neural structures contacting the extended primary cilium in the RMS and OB. In the RMS, each extended primary cilium made contact with a neighboring neuroblast (28/36 cells) or astrocyte (8/36 cells) (Fig. 7D–G). In the granule cell layer of the OB, the extended primary cilium of neuroblasts directly contacted neurites of mature neurons (14/14 cells). Close observation shows that each primary cilium of these neuroblasts was

making contact with the soma of granule cells (3/14 cells) or with presynaptic structures containing synaptic vesicles that had formed on the neurites (11/14 cells) (Fig. 7H–K). These results suggest that the extended primary cilium in a neuroblast interacts with its surrounding cells during migration in the RMS and OB.

Finally, we analyzed the dynamics of MT polymerization in each cellular domain during saltatory movement of cultured chain-forming neuroblasts, and compared the data with the orientation of the primary cilium analyzed using SBF-SEM. The highest polymerization levels of MTs labeled with EB3::GFP (Sawada et al., 2018) were observed in the distal leading process during leading-process extension phase, in the proximal leading process during the swelling-formation phase, and in the soma during somal translocation phase (Fig. 7L, Movie 13). On the other hand, quantification of ciliary orientation based on the SBF-SEM images (Fig. 6D', F', H', J') revealed that the majority of migrating neuroblasts (80–100%) of the leading-process extension and swelling-formation phases had a posteriorly oriented primary cilium regardless of the ciliary type, whereas migrating neuroblasts of the somal translocation phase had an anteriorly oriented primary cilium (Fig. 7M). The orientation of the primary cilium in the direction opposite to the cellular domain with the highest levels of MT polymerization suggests that ciliary orientation is related to the difference in the local MT polymerization levels in each migration phase rather than to ciliary maturation states.

Discussion

SBF-SEM analyses of migrating neuroblasts and the primary cilium *in vivo*

Time-lapse imaging of V-SVZ-derived migrating neuroblasts reveals each step of their saltatory movement (Ota et al., 2014; Sawada et al., 2018; Schaar and McConnell, 2005; Shinohara et al., 2012). Here, by analyzing the presence/absence of swelling and growth cone morphology, we could identify the migration phases of immature neuroblasts both in time-lapse imaging and in SBF-SEM analyses. Moreover, 3D reconstruction of mitochondria showed changes in their distribution in migration phases, which is consistent with a previous study in MGE-derived cortical interneurons (Lin-Hendel et al., 2016). Since dynamic changes in cellular morphology in migrating neuroblasts are supported by mitochondrial ATP production (Lin-Hendel et al., 2016), it is possible that mitochondria accumulate in subcellular regions with high energy demands such as the swelling.

SBF-SEM or another type of 3D-SEM, focused ion beam-SEM, have previously been used to analyze the fine morphology of the primary cilium (Insinna et al., 2019; Paridaen et al., 2013) and the molecular mechanisms of ciliogenesis (Buskin et al., 2018; David et al., 2014). Although our SBF-SEM analyses could not clearly visualize MT structures, we successfully identified primary cilium structures by detecting their basal bodies and associated membrane structures, whose electron density was strengthened by the reduced osmium-thiocarbohydrazide-osmium method (Seligman et al., 1966; Willingham and Rutherford, 1984). Our ultrastructural SBF-SEM images for different stages of ciliogenesis should provide a basis for analysis of the primary cilium in other cells in the brain or in other tissues under physiological and pathological conditions.

Unique morphology and dynamics of the primary cilium in V-SVZ-derived migrating neuroblasts

In contrast to other immature neurons migrating in the developing brain, the V-SVZ-derived neuroblasts are unique in that they are still mitotic and migrating in a chain in the RMS. Our observations suggest that ciliogenesis in migrating neuroblasts is transiently suppressed during mitosis (Fig. 8A), as reported in other mitotic cells (Malicki and Johnson, 2017). In addition, a small portion of proliferating

771 Dcx+ cells has an Arl13b+ primary cilium even in the M phase. It is possible that the
772 status of the primary cilium in migrating neuroblasts is influenced by dynamic
773 changes in their cellular circumstances, including those in the cell cycle and
774 saltatory movement.
775 Our live imaging and EM analyses revealed that migrating neuroblasts in
776 the postnatal RMS possess a primary cilium in the cytosol, which is transiently
777 extended from the cell surface prior to somal translocation (Fig. 8B). Similar
778 subcellular translocation of the primary cilium during migration has been reported in
779 MGE-derived interneurons (Baudoin et al., 2012), suggesting that ciliogenesis in
780 interneurons is regulated by common mechanisms in the embryonic and postnatal
781 brain. Interestingly, the “non-extended” primary cilium in immature neuroblasts
782 appeared to have access to the extracellular environment, which has been reported
783 in other types of mature cells (Dahl, 1967; Mazo et al., 2016; Smith et al., 1969;
784 Sorokin, 1962).
785 In MGE-derived migrating interneurons, extracellular extension of the
786 primary cilium could be regulated by fusion and fission of Golgi-derived ciliary
787 vesicles (Baudoin et al., 2012). A recent study suggests that the submerged state of
788 the primary cilium in the cytosol is maintained by association of daughter centriole
789 with the Golgi apparatus in retinal pigmental epithelial cells (Mazo et al., 2016). It
790 remains unknown whether these mechanisms are involved in maintenance of the
791 non-extended state of the primary cilium in postnatal-born migrating neuroblasts.
792 The FLP-bearing individual neuroblasts decelerating in the OB restrict
793 forward movement of the primary cilium in the leading process and promote cilium
794 extension from the cell surface (Fig. 8C), which is distinct from chain-forming
795 neuroblasts in the RMS. These changes in primary cilium dynamics may be related
796 to termination of migration and initiation of differentiation in the OB, which are
797 suppressed by homophilic chain formation and/or efficient migration in the RMS.
798
799 **Possible functions of the primary cilium in V-SVZ-derived migrating**
800 **neuroblasts**
801 Our SBF-SEM results showed that 88% of immature neuroblasts in the
802 adult RMS possess ciliary structures on their mother centrioles. Moreover, MTs
803 were observed to be extended radially from the basal body of the primary cilium in
804 migrating neuroblasts. Similar relationships between MTs and the basal body of the

primary cilium have also been reported in fibroblasts (Albrecht-Buehler and Bushnell, 1980; Schroder et al., 2011) and enteric neurons (Luesma et al., 2013). These findings suggest that the basal body of the primary cilium acts as an MTOC in the V-SVZ-derived migrating neuroblasts, which is consistent with previous studies (Baudoin et al., 2012; Tsai et al., 2007).

We found that the primary cilium orients posteriorly when neuroblasts actively polymerize MTs in the leading process, whereas it orients anteriorly when neuroblasts actively form a perinuclear MT cage (Fig. 8B). Thus, it is possible that active MT polymerization generates traction force that pulls the basal body, which would affect the ciliary orientation during saltatory movement. During neuroblast deceleration, the FLP induces local MT reorganization in the proximal leading process, which can decrease the MT polymerization-based traction force and sustain extension of the primary cilium in FLP-bearing neuroblasts. Taken together, these results suggest that the dynamics of the basal body and primary cilium are regulated by MT dynamics in saltatory movement of migrating neuroblasts.

Kif3A promotes ciliogenesis by regulating axoneme elongation and subdistal appendage formation in the basal body (Kodani et al., 2013). However, Kif3A also has non-ciliary functions such as transport of N-cadherin (Ichinose et al., 2015; Teng et al., 2005) and modulation of Wnt signaling (Corbit et al., 2008). Therefore, defective neuroblast migration caused by dnKif3A expression does not directly indicate the function of the primary cilium in neuroblast migration in the RMS. The KD of IFT88, which contributes to ciliogenesis independently of Kif3A (Pazour et al., 2000), also disrupted migration of V-SVZ-derived neuroblasts, similar to MGE-derived cortical interneurons (Baudoin et al., 2012). However, since the V-SVZ-derived migrating neuroblasts are mitotic, non-ciliary functions of IFT88 during mitosis including the regulation of spindle orientation (Borovina and Ciruna, 2013; Delaval et al., 2011; Robert et al., 2007) may affect neuronal distribution. Thus, our results suggest that disrupted neuroblast migration resulting from inhibition of Kif3A and IFT88 is, at least in part, attributable to the defects of primary cilium function in the V-SVZ-derived migrating neuroblasts.

The primary cilium contains signaling receptors such as Smoothened and 5HT6 on its membrane, which act as chemical sensors to regulate migration and maturation of cortical interneurons (Baudoin et al., 2012; Guo et al., 2017; Higginbotham et al., 2012; Riccio et al., 2009). Shh signaling promotes neuroblast

migration in the V-SVZ (Angot et al., 2008). Moreover, a recent study suggests that serotonin controls speed and directionality of the V-SVZ-derived migrating neuroblasts (Garcia-Gonzalez et al., 2017). While 5HT6::GFP localized only in the primary cilium, 5HT3A::GFP was detectable not only in the cilium but also in the cell body (Fig. 1J, L). Furthermore, 5HT6 and 5HT3A are a G protein-coupled receptor and a ligand-gated ion channel, respectively (Derkach et al., 1989; Monsma et al., 1993; Ruat et al., 1993). Therefore, it is possible that these two types of serotonin receptors coordinately regulate neuroblast migration in the adult RMS and OB via distinct signaling pathways. Serotonin fibers extending along the RMS-OB pathway (Garcia-Gonzalez et al., 2017) and the presence of a primary cilium in migrating neuroblasts are widely conserved among vertebrates. Since the postnatal-born neuroblasts must migrate over a long distance within the mature neuronal circuitry, which is distinct from embryonic neurons, they may need to continuously sense extracellular cues through the primary cilium for their efficient migration.

Migration and maturation of neuroblasts in the OB are affected by both olfactory (Petreanu and Alvarez-Buylla, 2002; Saghatelyan et al., 2004; Yamaguchi and Mori, 2005) and centrifugal (Garcia-Gonzalez et al., 2017; Kaneko et al., 2006) inputs. Interestingly, the extended primary cilium in individually migrating neuroblasts made direct contact with presynaptic structures in the OB (Fig. 7J–K). If the extended primary cilium has the potential to transduce electrical activity, as in the renal collecting duct epithelium (Liu et al., 2018), it may contribute to activity-dependent neuroblast migration and maturation in the OB.

Although the primary cilium has also been proposed to act as a mechanosensor (Malicki and Johnson, 2017), it remains unknown whether the primary cilium in migrating neuroblasts mediates mechanosensing. In retinal pigment epithelial cells, while the submerged primary cilium was not affected by fluid flow, the surfaced primary cilium, induced by *C-Nap1*/*CEP128* deficiencies, bent in response to fluid flow (Mazo et al., 2016). If the primary cilium in migrating neuroblasts is able to transduce mechanostimulation, its activity could be altered between non-extended and extended states, and affected by cell-cell contact that changes dynamically during chain migration.

In conclusion, this study suggests that primary cilium dynamics is related to the proliferation and saltatory movement of V-SVZ-derived migrating neuroblasts.

Our detailed description of the ultrastructural features and dynamics of primary cilium in migrating neuroblasts will be useful for future studies, which will clarify the functional significance of the primary cilium and novel regulatory mechanisms for neuroblast migration.

References

Albrecht-Buehler, G., and Bushnell, A. (1980) The ultrastructure of primary cilia in quiescent 3T3 cells, *Exp Cell Res* **126**, 427-437.

Amador-Arjona, A., Elliott, J., Miller, A., Ginbey, A., Pazour, G.J., Enikolopov, G., Roberts, A.J., and Terskikh, A.V. (2011) Primary cilia regulate proliferation of amplifying progenitors in adult hippocampus: implications for learning and memory, *J Neurosci* **31**, 9933-9944.

Angot, E., Loulier, K., Nguyen-Ba-Charvet, K.T., Gadeau, A.P., Ruat, M., and Traiffort, E. (2008) Chemoattractive activity of sonic hedgehog in the adult subventricular zone modulates the number of neural precursors reaching the olfactory bulb, *Stem Cells* **26**, 2311-2320.

Arellano, J.I., Guadiana, S.M., Breunig, J.J., Rakic, P., and Sarkisian, M.R. (2012) Development and distribution of neuronal cilia in mouse neocortex, *J Comp Neurol* **520**, 848-873.

Arvidsson, A., Collin, T., Kirik, D., Kokaia, Z., and Lindvall, O. (2002) Neuronal replacement from endogenous precursors in the adult brain after stroke, *Nat Med* **8**, 963-970.

Baudoin, J.P., Viou, L., Launay, P.S., Luccardini, C., Espeso Gil, S., Kiyasova, V., Irinopoulou, T., Alvarez, C., Rio, J.P., Boudier, T., et al. (2012) Tangentially migrating neurons assemble a primary cilium that promotes their reorientation to the cortical plate, *Neuron* **76**, 1108-1122.

Belevich, I., Joensuu, M., Kumar, D., Vihinen, H., and Jokitalo, E. (2016) Microscopy Image Browser: A Platform for Segmentation and Analysis of Multidimensional Datasets, *PLoS Biol* **14**, e1002340.

Bellion, A., Baudoin, J.P., Alvarez, C., Bornens, M., and Metin, C. (2005) Nucleokinesis in tangentially migrating neurons comprises two alternating phases: forward migration of the Golgi/centrosome associated with centrosome splitting and myosin contraction at the rear, *J Neurosci* **25**, 5691-5699.

Belvindrah, R., Nissant, A., and Lledo, P.M. (2011) Abnormal neuronal migration changes the fate of developing neurons in the postnatal olfactory bulb, *J Neurosci* **31**, 7551-7562.

Bishop, G.A., Berbari, N.F., Lewis, J., and Mykytyn, K. (2007) Type III adenylyl

912 cyclase localizes to primary cilia throughout the adult mouse brain, *J Comp*
913 *Neurol* **505**, 562-571.
914 Borovina, A., and Ciruna, B. (2013) IFT88 plays a cilia- and PCP-independent role
915 in controlling oriented cell divisions during vertebrate embryonic
916 development, *Cell Rep* **5**, 37-43.
917 Brailov, I., Bancila, M., Brisorgueil, M.J., Miquel, M.C., Hamon, M., and Verge, D.
918 (2000) Localization of 5-HT(6) receptors at the plasma membrane of
919 neuronal cilia in the rat brain, *Brain Res* **872**, 271-275.
920 Breunig, J.J., Sarkisian, M.R., Arellano, J.I., Morozov, Y.M., Ayoub, A.E., Sojitra, S.,
921 Wang, B., Flavell, R.A., Rakic, P., and Town, T. (2008) Primary cilia regulate
922 hippocampal neurogenesis by mediating sonic hedgehog signaling, *Proc*
923 *Natl Acad Sci U S A* **105**, 13127-13132.
924 Briggman, K.L., and Bock, D.D. (2012) Volume electron microscopy for neuronal
925 circuit reconstruction, *Curr Opin Neurobiol* **22**, 154-161.
926 Buskin, A., Zhu, L., Chichagova, V., Basu, B., Mozaffari-Jovin, S., Dolan, D., Droop,
927 A., Collin, J., Bronstein, R., Mehrotra, S., et al. (2018) Disrupted alternative
928 splicing for genes implicated in splicing and ciliogenesis causes PRPF31
929 retinitis pigmentosa, *Nat Commun* **9**, 4234.
930 Capilla-Gonzalez, V., Cebrian-Silla, A., Guerrero-Cazares, H., Garcia-Verdugo, J.M.,
931 and Quinones-Hinojosa, A. (2014) Age-related changes in astrocytic and
932 ependymal cells of the subventricular zone, *Glia* **62**, 790-803.
933 Caspary, T., Larkins, C.E., and Anderson, K.V. (2007) The graded response to
934 Sonic Hedgehog depends on cilia architecture, *Dev Cell* **12**, 767-778.
935 Chen, J.L., Chang, C.H., and Tsai, J.W. (2019) Gli2 Rescues Delays in Brain
936 Development Induced by Kif3a Dysfunction, *Cereb Cortex* **29**, 751-764.
937 Corbit, K.C., Shyer, A.E., Dowdle, W.E., Gaulden, J., Singla, V., Chen, M.H.,
938 Chuang, P.T., and Reiter, J.F. (2008) Kif3a constrains
939 beta-catenin-dependent Wnt signalling through dual ciliary and non-ciliary
940 mechanisms, *Nat Cell Biol* **10**, 70-76.
941 Dahl, H.A. (1967) On the cilium cell relationship in the adenohypophysis of the
942 mouse, *Z Zellforsch Mikrosk Anat* **83**, 169-177.
943 Danilov, A.I., Gomes-Leal, W., Ahlenius, H., Kokaia, Z., Carlemalm, E., and Lindvall,
944 O. (2009) Ultrastructural and antigenic properties of neural stem cells and
945 their progeny in adult rat subventricular zone, *Glia* **57**, 136-152.

946 David, A., Liu, F., Tibelius, A., Vulprecht, J., Wald, D., Rothermel, U., Ohana, R.,
947 Seitel, A., Metzger, J., Ashery-Padan, R., et al. (2014) Lack of centrioles and
948 primary cilia in STIL(-/-) mouse embryos, *Cell Cycle* **13**, 2859-2868.
949 Delaval, B., Bright, A., Lawson, N.D., and Doxsey, S. (2011) The cilia protein IFT88
950 is required for spindle orientation in mitosis, *Nat Cell Biol* **13**, 461-468.
951 Denk, W., Briggman, K.L., and Helmstaedter, M. (2012) Structural neurobiology:
952 missing link to a mechanistic understanding of neural computation, *Nat Rev*
953 *Neurosci* **13**, 351-358.
954 Derkach, V., Surprenant, A., and North, R.A. (1989) 5-HT3 receptors are membrane
955 ion channels, *Nature* **339**, 706-709.
956 Doetsch, F., García-Verdugo, J.M., and Alvarez-Buylla, A. (1997) Cellular
957 composition and three-dimensional organization of the subventricular
958 germinal zone in the adult mammalian brain, *J Neurosci* **17**, 5046-5061.
959 Ford, M.J., Yeyati, P.L., Mali, G.R., Keighren, M.A., Waddell, S.H., Mjoseng, H.K.,
960 Douglas, A.T., Hall, E.A., Sakaue-Sawano, A., Miyawaki, A., et al. (2018) A
961 Cell/Cilia Cycle Biosensor for Single-Cell Kinetics Reveals Persistence of
962 Cilia after G1/S Transition Is a General Property in Cells and Mice, *Dev Cell*
963 **47**, 509-523 e505.
964 Fujikake, K., Sawada, M., Hikita, T., Seto, Y., Kaneko, N., Herranz-Perez, V., Dohi,
965 N., Homma, N., Osaga, S., Yanagawa, Y., et al. (2018) Detachment of
966 Chain-Forming Neuroblasts by Fyn-Mediated Control of cell-cell Adhesion in
967 the Postnatal Brain, *J Neurosci* **38**, 4598-4609.
968 Garcia-Gonzalez, D., Khodosevich, K., Watanabe, Y., Rollenhagen, A., Lubke,
969 J.H.R., and Monyer, H. (2017) Serotonergic Projections Govern Postnatal
970 Neuroblast Migration, *Neuron* **94**, 534-549 e539.
971 Guadiana, S.M., Semple-Rowland, S., Daroszewski, D., Madorsky, I., Breunig, J.J.,
972 Mykytyn, K., and Sarkisian, M.R. (2013) Arborization of dendrites by
973 developing neocortical neurons is dependent on primary cilia and type 3
974 adenylyl cyclase, *J Neurosci* **33**, 2626-2638.
975 Guemez-Gamboa, A., Coufal, N.G., and Gleeson, J.G. (2014) Primary cilia in the
976 developing and mature brain, *Neuron* **82**, 511-521.
977 Guo, J., Otis, J.M., Higginbotham, H., Monckton, C., Cheng, J., Asokan, A., Mykytyn,
978 K., Caspary, T., Stuber, G.D., and Anton, E.S. (2017) Primary Cilia Signaling
979 Shapes the Development of Interneuronal Connectivity, *Dev Cell* **42**,

286-300 e284.

Han, Y.G., Spassky, N., Romaguera-Ros, M., Garcia-Verdugo, J.M., Aguilar, A., Schneider-Maunoury, S., and Alvarez-Buylla, A. (2008) Hedgehog signaling and primary cilia are required for the formation of adult neural stem cells, *Nat Neurosci* **11**, 277-284.

Higginbotham, H., Bielas, S., Tanaka, T., and Gleeson, J.G. (2004) Transgenic mouse line with green-fluorescent protein-labeled Centrin 2 allows visualization of the centrosome in living cells, *Transgenic Res* **13**, 155-164.

Higginbotham, H., Eom, T.Y., Mariani, L.E., Bachleda, A., Hirt, J., Gukassyan, V., Cusack, C.L., Lai, C., Caspary, T., and Anton, E.S. (2012) Arl13b in primary cilia regulates the migration and placement of interneurons in the developing cerebral cortex, *Dev Cell* **23**, 925-938.

Hikita, T., Ohno, A., Sawada, M., Ota, H., and Sawamoto, K. (2014) Rac1-mediated indentation of resting neurons promotes the chain migration of new neurons in the rostral migratory stream of post-natal mouse brain, *J Neurochem* **128**, 790-797.

Ichinose, S., Ogawa, T., and Hirokawa, N. (2015) Mechanism of Activity-Dependent Cargo Loading via the Phosphorylation of KIF3A by PKA and CaMKIIa, *Neuron* **87**, 1022-1035.

Ikeda, M., Hirota, Y., Sakaguchi, M., Yamada, O., Kida, Y.S., Ogura, T., Otsuka, T., Okano, H., and Sawamoto, K. (2010) Expression and proliferation-promoting role of Diversin in the neuronally committed precursor cells migrating in the adult mouse brain, *Stem Cells* **28**, 2017-2026.

Insinna, C., Lu, Q., Teixeira, I., Harned, A., Semler, E.M., Stauffer, J., Magidson, V., Tiwari, A., Kenworthy, A.K., Narayan, K., et al. (2019) Investigation of F-BAR domain PACSIN proteins uncovers membrane tubulation function in cilia assembly and transport, *Nat Commun* **10**, 428.

Inta, D., Alfonso, J., von Engelhardt, J., Kreuzberg, M.M., Meyer, A.H., van Hooft, J.A., and Monyer, H. (2008) Neurogenesis and widespread forebrain migration of distinct GABAergic neurons from the postnatal subventricular zone, *Proc Natl Acad Sci U S A* **105**, 20994-20999.

Jinnou, H., Sawada, M., Kawase, K., Kaneko, N., Herranz-Pérez, V., Miyamoto, T., Kawaue, T., Miyata, T., Tabata, Y., Akaike, T., et al. (2018) Radial glial fibers support neuronal migration and regeneration after neonatal brain injury, *Cell*

1014 *Stem Cell* **22**, 128-137.
1015 Kanda, Y. (2013) Investigation of the freely available easy-to-use software 'EZR' for
1016 medical statistics, *Bone Marrow Transplant* **48**, 452-458.
1017 Kaneko, N., Herranz-Perez, V., Otsuka, T., Sano, H., Ohno, N., Omata, T., Nguyen,
1018 H.B., Thai, T.Q., Nambu, A., Kawaguchi, Y., et al. (2018) New neurons use
1019 Slit-Robo signaling to migrate through the glial meshwork and approach a
1020 lesion for functional regeneration, *Sci Adv* **4**, eaav0618.
1021 Kaneko, N., Okano, H., and Sawamoto, K. (2006) Role of the cholinergic system in
1022 regulating survival of newborn neurons in the adult mouse dentate gyrus and
1023 olfactory bulb, *Genes Cells* **11**, 1145-1159.
1024 Khodosevich, K., Lazarini, F., von Engelhardt, J., Kaneko, H., Lledo, P.M., and
1025 Monyer, H. (2013) Connective tissue growth factor regulates interneuron
1026 survival and information processing in the olfactory bulb, *Neuron* **79**,
1027 1136-1151.
1028 Khodosevich, K., Seeburg, P.H., and Monyer, H. (2009) Major signaling pathways in
1029 migrating neuroblasts, *Front Mol Neurosci* **2**, 7.
1030 Khodosevich, K., Zuccotti, A., Kreuzberg, M.M., Le Magueresse, C., Frank, M.,
1031 Willecke, K., and Monyer, H. (2012) Connexin45 modulates the proliferation
1032 of transit-amplifying precursor cells in the mouse subventricular zone, *Proc*
1033 *Natl Acad Sci U S A* **109**, 20107-20112.
1034 Kishimoto, N., Alfaro-Cervello, C., Shimizu, K., Asakawa, K., Urasaki, A., Nonaka,
1035 S., Kawakami, K., Garcia-Verdugo, J.M., and Sawamoto, K. (2011) Migration
1036 of neuronal precursors from the telencephalic ventricular zone into the
1037 olfactory bulb in adult zebrafish, *J Comp Neurol* **519**, 3549-3565.
1038 Kishimoto, N., Asakawa, K., Madelaine, R., Blader, P., Kawakami, K., and
1039 Sawamoto, K. (2013) Interhemispheric asymmetry of olfactory
1040 input-dependent neuronal specification in the adult brain, *Nat Neurosci* **16**,
1041 884-888.
1042 Kodani, A., Salome Sirerol-Piquer, M., Seol, A., Garcia-Verdugo, J.M., and Reiter,
1043 J.F. (2013) Kif3a interacts with Dynactin subunit p150 Glued to organize
1044 centriole subdistal appendages, *EMBO J* **32**, 597-607.
1045 Kreuzberg, M., Kanov, E., Timofeev, O., Schwaninger, M., Monyer, H., and
1046 Khodosevich, K. (2010) Increased subventricular zone-derived cortical
1047 neurogenesis after ischemic lesion, *Exp Neurol* **226**, 90-99.

1048 Kumamoto, N., Gu, Y., Wang, J., Janoschka, S., Takemaru, K., Levine, J., and Ge,
1049 S. (2012) A role for primary cilia in glutamatergic synaptic integration of
1050 adult-born neurons, *Nat Neurosci* **15**, 399-405, S391.
1051 Lin-Hendel, E.G., McManus, M.J., Wallace, D.C., Anderson, S.A., and Golden, J.A.
1052 (2016) Differential Mitochondrial Requirements for Radially and Non-radially
1053 Migrating Cortical Neurons: Implications for Mitochondrial Disorders, *Cell*
1054 *Rep* **15**, 229-237.
1055 Liu, X., Vien, T., Duan, J., Sheu, S.H., DeCaen, P.G., and Clapham, D.E. (2018)
1056 Polycystin-2 is an essential ion channel subunit in the primary cilium of the
1057 renal collecting duct epithelium, *Elife* **7**.
1058 Lois, C., and Alvarez-Buylla, A. (1994) Long-distance neuronal migration in the
1059 adult mammalian brain, *Science* **264**, 1145-1148.
1060 Lois, C., Garcia-Verdugo, J.M., and Alvarez-Buylla, A. (1996) Chain migration of
1061 neuronal precursors, *Science* **271**, 978-981.
1062 Luesma, M.J., Cantarero, I., Castiella, T., Soriano, M., Garcia-Verdugo, J.M., and
1063 Junquera, C. (2013) Enteric neurons show a primary cilium, *J Cell Mol Med*
1064 **17**, 147-153.
1065 Luo, J., Chen, X., Pan, Y.W., Lu, S., Xia, Z., and Storm, D.R. (2015) The type 3
1066 adenylyl cyclase is required for the survival and maturation of newly
1067 generated granule cells in the olfactory bulb, *PLoS One* **10**, e0122057.
1068 Luskin, M.B. (1993) Restricted proliferation and migration of postnatally generated
1069 neurons derived from the forebrain subventricular zone, *Neuron* **11**, 173-189.
1070 Madisen, L., Zwingman, T.A., Sunkin, S.M., Oh, S.W., Zariwala, H.A., Gu, H., Ng,
1071 L.L., Palmiter, R.D., Hawrylycz, M.J., Jones, A.R., et al. (2010) A robust and
1072 high-throughput Cre reporting and characterization system for the whole
1073 mouse brain, *Nat Neurosci* **13**, 133-140.
1074 Malicki, J.J., and Johnson, C.A. (2017) The Cilium: Cellular Antenna and Central
1075 Processing Unit, *Trends Cell Biol* **27**, 126-140.
1076 Mazo, G., Soplop, N., Wang, W.J., Uryu, K., and Tsou, M.F. (2016) Spatial Control
1077 of Primary Ciliogenesis by Subdistal Appendages Alters
1078 Sensation-Associated Properties of Cilia, *Dev Cell* **39**, 424-437.
1079 Menn, B., Garcia-Verdugo, J.M., Yaschine, C., Gonzalez-Perez, O., Rowitch, D.,
1080 and Alvarez-Buylla, A. (2006) Origin of oligodendrocytes in the subventricular
1081 zone of the adult brain, *J Neurosci* **26**, 7907-7918.

1082 Monsma, F.J., Jr., Shen, Y., Ward, R.P., Hamblin, M.W., and Sibley, D.R. (1993)
1083 Cloning and expression of a novel serotonin receptor with high affinity for
1084 tricyclic psychotropic drugs, *Mol Pharmacol* **43**, 320-327.
1085 Nakamuta, S., Yang, Y.T., Wang, C.L., Gallo, N.B., Yu, J.R., Tai, Y., and Van Aelst, L.
1086 (2017) Dual role for DOCK7 in tangential migration of interneuron precursors
1087 in the postnatal forebrain, *J Cell Biol* **216**, 4313-4330.
1088 Nguyen, H.B., Thai, T.Q., Saitoh, S., Wu, B., Saitoh, Y., Shimo, S., Fujitani, H.,
1089 Otobe, H., and Ohno, N. (2016) Conductive resins improve charging and
1090 resolution of acquired images in electron microscopic volume imaging, *Sci*
1091 *Rep* **6**, 23721.
1092 Obernier, K., and Alvarez-Buylla, A. (2019) Neural stem cells: origin, heterogeneity
1093 and regulation in the adult mammalian brain, *Development* **146**.
1094 Ogino, T., Sawada, M., Takase, H., Nakai, C., Herranz-Perez, V., Cebrian-Silla, A.,
1095 Kaneko, N., Manuel Garcia-Verdugo, J., and Sawamoto, K. (2016)
1096 Characterization of multiciliated ependymal cells that emerge in the
1097 neurogenic niche of the aged zebrafish brain, *J Comp Neurol*.
1098 Ohno, N., Katoh, M., Saitoh, Y., Saitoh, S., and Ohno, S. (2015) Three-dimensional
1099 volume imaging with electron microscopy toward connectome, *Microscopy*
1100 *(Oxf)* **64**, 17-26.
1101 Ota, H., Hikita, T., Sawada, M., Nishioka, T., Matsumoto, M., Komura, M., Ohno, A.,
1102 Kamiya, Y., Miyamoto, T., Asai, N., et al. (2014) Speed control for neuronal
1103 migration in the postnatal brain by Gmip-mediated local inactivation of RhoA,
1104 *Nat Commun* **5**, 4532.
1105 Parent, J.M., Vexler, Z.S., Gong, C., Derugin, N., and Ferriero, D.M. (2002) Rat
1106 forebrain neurogenesis and striatal neuron replacement after focal stroke,
1107 *Ann Neurol* **52**, 802-813.
1108 Paridaen, J.T., Wilsch-Brauninger, M., and Huttner, W.B. (2013) Asymmetric
1109 inheritance of centrosome-associated primary cilium membrane directs
1110 ciliogenesis after cell division, *Cell* **155**, 333-344.
1111 Pazour, G.J., Dickert, B.L., Vucica, Y., Seeley, E.S., Rosenbaum, J.L., Witman, G.B.,
1112 and Cole, D.G. (2000) Chlamydomonas IFT88 and its mouse homologue,
1113 polycystic kidney disease gene tg737, are required for assembly of cilia and
1114 flagella, *J Cell Biol* **151**, 709-718.
1115 Petreanu, L., and Alvarez-Buylla, A. (2002) Maturation and death of adult-born

olfactory bulb granule neurons: role of olfaction, *J Neurosci* **22**, 6106-6113.

Ponti, G., Obernier, K., Guinto, C., Jose, L., Bonfanti, L., and Alvarez-Buylla, A. (2013) Cell cycle and lineage progression of neural progenitors in the ventricular-subventricular zones of adult mice, *Proc Natl Acad Sci U S A* **110**, E1045-1054.

Riccio, O., Potter, G., Walzer, C., Vallet, P., Szabo, G., Vutskits, L., Kiss, J.Z., and Dayer, A.G. (2009) Excess of serotonin affects embryonic interneuron migration through activation of the serotonin receptor 6, *Mol Psychiatry* **14**, 280-290.

Robert, A., Margall-Ducos, G., Guidotti, J.E., Bregerie, O., Celati, C., Brechot, C., and Desdouets, C. (2007) The intraflagellar transport component IFT88/polaris is a centrosomal protein regulating G1-S transition in non-ciliated cells, *J Cell Sci* **120**, 628-637.

Ruat, M., Traiffort, E., Arrang, J.M., Tardivel-Lacombe, J., Diaz, J., Leurs, R., and Schwartz, J.C. (1993) A novel rat serotonin (5-HT6) receptor: molecular cloning, localization and stimulation of cAMP accumulation, *Biochem Biophys Res Commun* **193**, 268-276.

Saghatelyan, A., de Chevigny, A., Schachner, M., and Lledo, P.M. (2004) Tenascin-R mediates activity-dependent recruitment of neuroblasts in the adult mouse forebrain, *Nat Neurosci* **7**, 347-356.

Sawada, M., Ohno, N., Kawaguchi, M., Huang, S.H., Hikita, T., Sakurai, Y., Bang Nguyen, H., Quynh Thai, T., Ishido, Y., Yoshida, Y., et al. (2018) PlexinD1 signaling controls morphological changes and migration termination in newborn neurons, *EMBO J* **37**, e97404.

Sawamoto, K., Wichterle, H., Gonzalez-Perez, O., Cholfin, J.A., Yamada, M., Spassky, N., Murcia, N.S., Garcia-Verdugo, J.M., Marin, O., Rubenstein, J.L., et al. (2006) New neurons follow the flow of cerebrospinal fluid in the adult brain, *Science* **311**, 629-632.

Schaar, B.T., and McConnell, S.K. (2005) Cytoskeletal coordination during neuronal migration, *Proc Natl Acad Sci U S A* **102**, 13652-13657.

Schroder, J.M., Larsen, J., Komarova, Y., Akhmanova, A., Thorsteinsson, R.I., Grigoriev, I., Manguso, R., Christensen, S.T., Pedersen, S.F., Geimer, S., et al. (2011) EB1 and EB3 promote cilia biogenesis by several centrosome-related mechanisms, *J Cell Sci* **124**, 2539-2551.

1150 Seki, T., and Arai, Y. (1991) The persistent expression of a highly polysialylated
1151 NCAM in the dentate gyrus of the adult rat, *Neurosci Res* **12**, 503-513.
1152 Seligman, A.M., Wasserkrug, H.L., and Hanker, J.S. (1966) A new staining method
1153 (OTO) for enhancing contrast of lipid--containing membranes and droplets in
1154 osmium tetroxide--fixed tissue with osmiophilic thiocarbohydrazide(TCH), *J*
1155 *Cell Biol* **30**, 424-432.
1156 Shinohara, R., Thumkeo, D., Kamijo, H., Kaneko, N., Sawamoto, K., Watanabe, K.,
1157 Takebayashi, H., Kiyonari, H., Ishizaki, T., Furuyashiki, T., et al. (2012) A role
1158 for mDia, a Rho-regulated actin nucleator, in tangential migration of
1159 interneuron precursors, *Nat Neurosci* **15**, 373-380.
1160 Smith, J.W., Christie, K.N., and Frame, J. (1969) Desmosomes, cilia and
1161 acanthosomes associated with keratocytes, *J Anat* **105**, 383-392.
1162 Sorokin, S. (1962) Centrioles and the formation of rudimentary cilia by fibroblasts
1163 and smooth muscle cells, *J Cell Biol* **15**, 363-377.
1164 Teng, J., Rai, T., Tanaka, Y., Takei, Y., Nakata, T., Hirasawa, M., Kulkarni, A.B., and
1165 Hirokawa, N. (2005) The KIF3 motor transports N-cadherin and organizes
1166 the developing neuroepithelium, *Nat Cell Biol* **7**, 474-482.
1167 Thai, T.Q., Nguyen, H.B., Saitoh, S., Wu, B., Saitoh, Y., Shimo, S., Elewa, Y.H., Ichii,
1168 O., Kon, Y., Takaki, T., et al. (2016) Rapid specimen preparation to improve
1169 the throughput of electron microscopic volume imaging for three-dimensional
1170 analyses of subcellular ultrastructures with serial block-face scanning
1171 electron microscopy, *Med Mol Morphol* **49**, 154-162.
1172 Tong, C.K., Han, Y.G., Shah, J.K., Obernier, K., Guinto, C.D., and Alvarez-Buylla, A.
1173 (2014) Primary cilia are required in a unique subpopulation of neural
1174 progenitors, *Proc Natl Acad Sci U S A* **111**, 12438-12443.
1175 Trivedi, N., Ramahi, J.S., Karakaya, M., Howell, D., Kerekes, R.A., and Solecki, D.J.
1176 (2014) Leading-process actomyosin coordinates organelle positioning and
1177 adhesion receptor dynamics in radially migrating cerebellar granule neurons,
1178 *Neural Dev* **9**, 26.
1179 Tsai, J.W., Bremner, K.H., and Vallee, R.B. (2007) Dual subcellular roles for LIS1
1180 and dynein in radial neuronal migration in live brain tissue, *Nat Neurosci* **10**,
1181 970-979.
1182 Watanabe, T., Kakeno, M., Matsui, T., Sugiyama, I., Arimura, N., Matsuzawa, K.,
1183 Shirahige, A., Ishidate, F., Nishioka, T., Taya, S., et al. (2015) TTBK2 with

EB1/3 regulates microtubule dynamics in migrating cells through KIF2A phosphorylation, *J Cell Biol* **210**, 737-751.

Wheway, G., Nazlamova, L., and Hancock, J.T. (2018) Signaling through the Primary Cilium, *Front Cell Dev Biol* **6**, 8.

Willingham, M.C., and Rutherford, A.V. (1984) The use of osmium-thiocarbohydrazide-osmium (OTO) and ferrocyanide-reduced osmium methods to enhance membrane contrast and preservation in cultured cells, *J Histochem Cytochem* **32**, 455-460.

Yamaguchi, M., and Mori, K. (2005) Critical period for sensory experience-dependent survival of newly generated granule cells in the adult mouse olfactory bulb, *Proc Natl Acad Sci U S A* **102**, 9697-9702.

Yamashita, T., Ninomiya, M., Hernández Acosta, P., García-Verdugo, J.M., Sunabori, T., Sakaguchi, M., Adachi, K., Kojima, T., Hirota, Y., Kawase, T., et al. (2006) Subventricular zone-derived neuroblasts migrate and differentiate into mature neurons in the post-stroke adult striatum, *J Neurosci* **26**, 6627-6636.

Figure 1. Expression of ciliary markers in migrating neuroblasts in the RMS of the postnatal vertebrate brain.

(**A**–**A2'**) Representative images of RMS (A1, A1') and OB (A2, A2') sections of adult *GFP::Cent2* mice stained for GFP (green), Dcx (red), and Arl13b (white). The boxed areas in (A1 and A2) are enlarged in (A1' and A2'), respectively. Dcx+ neuroblasts have Arl13b+ structures (arrows) close to one of the pair of GFP::Cent2+ centrioles (arrowheads) in the RMS (A1') and OB (A2').

(**B**, **B'**) Representative image of tdTomato- and GFP::Cent2-labeled cells in the RMS. Lentivirus expressing GFP::Cent2 and Cre was injected into the V-SVZ of adult *R26-tdTomato* mice. A sagittal section of the RMS of *R26-tdTomato* mice at 6 days post-injection (dpi) stained for GFP (green), DsRed (red), and Arl13b (white, arrows) is shown. The boxed areas in (B) are enlarged in (B'). (B') An Arl13b+ structure (arrows) is located close to one of the pair of GFP::Cent2+ centrioles (arrowheads).

(**C**) Representative image of an RMS section in *5HT3A-EGFP* mice (Inta et al., 2008) stained for GFP (green) and adenylate cyclase III (ACIII, red). The arrow indicates an ACIII+ structure.

(**D**–**G**) Representative images of OB sections in WT mice stained for olfactory interneuron markers (green; D, parvalbumin [PV]; E, tyrosine hydroxylase [TH]; F, calretinin [CR]; G, calbindin [CB]) and ACIII (red). Arrows indicate ACIII+ structures in the olfactory interneurons. EPL, external plexiform layer; GL, glomerular layer.

(**H**–**J**) Localization of fluorescent protein-fused ciliary markers in migrating neuroblasts in the adult RMS. Arl13b::Venus (H), ACIII::GFP (I), or 5HT6::GFP (J) accumulated as spots (arrows) in the perinuclear region of Dcx+ neuroblasts. Dashed lines delineate the boundaries of individual nuclei. Blue, Hoechst 33342-stained nuclei.

(**K**–**M'**) Colocalization of GFP-fused 5HT3A and SSTR3 with ciliary markers in migrating neuroblasts in the adult RMS. Retroviruses expressing 5HT3A::GFP or neuroblasts expressing SSTR3::GFP were injected into the V-SVZ of adult WT mice (K). dpi, days post-injection. 5HT3A::GFP signal (L, green) is observed in the ACIII+ structure (L, arrow) in the adult RMS. SSTR3::GFP signal (M, M', green) is localized in the Arl13b+ structure (M, M', red) in the leading process of migrating neuroblasts in the RMS. The boxed area in (M) is enlarged in (M').

(**N**–**N’**) Representative images of a coronal RMS section of an adult zebrafish stained for PSA-NCAM (N, N’, red) and acetylated tubulin (N’, Ac-Tubulin, green). The boxed area in (N) is enlarged in (N’). Ac-Tubulin+ dots (N’, green, arrows) were observed in the PSA-NCAM+ immature neuroblasts in the adult zebrafish RMS. V, ventricle.

(**O**–**P’’**) Representative images of coronal RMS (O, DAPI) and OB (P, DAPI) sections of adult rhesus monkeys stained for Dcx (O’, P’, P’’, red) and Arl13b (O’, P’, P’’, green). Arl13b+ structures (O’, P’, P’’, arrows) were observed in the Dcx+ immature neuroblasts in the adult rhesus monkey RMS.

Scale bars: 5 μm (A1, A2, B, C, M, O’, P’, P’’), 2 μm (A1’, A2’, D–J, L, J, M’), 50 μm (N), 500 μm (P), 1 mm (O).

Figure 2. Primary cilium dynamics during saltatory movement of V-SVZ-derived cultured neuroblasts.

(**A**) Labeling of primary cilia and basal body in V-SVZ-derived cultured neuroblasts. Arl13b::Venus was introduced into V-SVZ cells dissected from postnatal day 0–1 (P0–1) *GFP::Cent2* mice. Two GFP::Cent2+ centrioles (green arrows) and an Arl13b::Venus+ primary cilium (yellow arrow) are visualized.

(**B**–**E'**) Time-lapse imaging of a cultured migrating neuroblast expressing GFP::Cent2 and Arl13b::Venus. Extension or non-extension of an Arl13b::Venus+ primary cilium from the cell surface is indicated below (B) by plus and minus signs, respectively. Boxed areas in (B, 10, 12, and 20 min) are shown orthogonally in (C–E). Boxed area in (B, 0 min) is enlarged in (A). Three-dimensional reconstructions (*y-z* view) of the neuroblast in (B, 10, 12, and 20 min) are shown (C'–E'). Yellow arrows indicate an extended primary cilium (D, D'). Opened and filled arrowheads (B) indicate spread and collapsed growth cones, respectively.

(**F**) Proportion of extension of a primary cilium from the cell surface during leading-process (LP) extension phase, swelling-formation phase, and somal translocation phase ($x^2_{(2)}$ = 30.679, p = 0.00000022, Friedman's test; LP extension phase vs swelling-formation phase, p = 0.00041, LP extension phase vs somal translocation phase, p = 0.0017, Wilcoxon signed rank test, adjusted with Bonferroni correction; n = 20 cells from eleven independent cultures prepared on different days).

(**G**–**J'**) Time-lapse imaging of a cultured FLP-bearing neuroblast expressing dTomato::Cent2 and Arl13b::Venus. Extension of an Arl13b::Venus+ primary cilium from the cell surface is indicated by a plus sign (G). The lower boxed area in (G, 0 min) is magnified above to visualize the Arl13b::Venus+ primary cilium and dTomato::Cent2+ basal body. Boxed areas in (G, 10, 20, and 24 min) are shown orthogonally in (H–J). Three-dimensional reconstructions (*y-z* view) of the neuroblast in (G, 10, 20, and 24 min) are shown (H'–J'). Yellow and white arrows indicate an extended primary cilium and FLP, respectively (H'–J').

Scale bars: 2 μm (A, B, G), 1 μm (C, D, E, H, I, J), 5 μm (C', D', E', H', I', J'). ***p < 0.005. Error bars indicate mean ± SEM.

Figure 3. Defects in ciliogenesis and saltatory movement of V-SVZ-derived migrating neuroblasts caused by expressing a dominant-negative form of Kif3A or IFT88 shRNA.

(**A**–**I**) Defects in ciliogenesis, orientation, and final positioning of V-SVZ-derived migrating neuroblasts caused by expressing a dominant-negative form of Kif3A (dnKif3A) (A–E, I) or IFT88 shRNA (F–H) in the adult RMS. Lentivirus encoding dnKif3A and Venus (A–E, I), or IFT88 shRNA and DsRed (F–H), was injected into the V-SVZ of WT mice. (A, B) Representative images of control (A, green) and dnKif3A-expressing (B, green) cells in the adult RMS. An Arl13b+ primary cilium (red, arrow in the enlarged box in [A]) was observed in the control but not the dnKif3A-expressing migrating neuroblasts. (C) Proportion of Arl13b+ primary cilium-bearing neuroblasts in the control and dnKif3A-expressing groups at 7 days post-infection (dpi) ($t_{(4)} = 15.76$, $p = 9.5 \times 10^{-5}$, unpaired *t*-test; n = 3 mice each). (D) Distribution of labeled neuroblasts in the OB of control and dnKif3A-expressing groups at 7 dpi ($t_{(6)} = 3.62$, $p = 0.011$, unpaired *t*-test; n = 4 mice each). (E) Orientation of labeled neuroblasts in the control and dnKif3A-expressing groups at 7 dpi ($F_{group(1,6)} = 0.0003$, $p_{group} = 0.99$, $F_{orientation(2,12)} = 79.8$, $p_{orientation} = 1.2 \times 10^{-7}$, $F_{group \times orientation(2,12)} = 21.8$, $p_{group \times orientation} = 0.00010$, two-way repeated-measures ANOVA; control vs dnKif3A, $t_{(6)} = 5.0$, $p = 0.0074$ in forward orientation; $t_{(6)} = –4.89$, $p = 0.0082$ in backward orientation; unpaired *t*-test; n = 4 mice each). (F) Proportion of Arl13b+ primary cilium-bearing neuroblasts in the control and IFT88-knockdown (KD) groups at 7 dpi ($t_{(4)} = 17.3$, $p = 6.6 \times 10^{-5}$, unpaired *t*-test; n = 3 mice each). (G) Distribution of labeled neuroblasts in the OB of control and IFT88-KD groups at 7 dpi ($t_{(5)} = 2.92$, $p = 0.033$, unpaired *t*-test; control, n = 3 mice; IFT88-KD, n = 4 mice). (H) Orientation of labeled neuroblasts in the control and IFT88-KD groups at 7 dpi ($F_{group(1,5)} = 0.056$, $p_{group} = 0.82$, $F_{orientation(2,10)} = 1101.8$, $p_{orientation} = 1.9 \times 10^{-12}$, $F_{group \times orientation(2,10)} = 34.0$, $p_{group \times orientation} = 3.5 \times 10^{-5}$, two-way repeated-measures ANOVA; control vs IFT88-KD, $t_{(5)} = 6.0$, $p = 0.0054$ in forward orientation; $t_{(5)} = –5.86$, $p = 0.0061$ in backward orientation; unpaired *t*-test; control, n = 3 mice; IFT88-KD, n = 4 mice).

(I) The final positioning of labeled neuroblasts in the OB and RMS of control and dnKif3A-expressing groups at 14 dpi ($F_{group(1,6)} = –0.0001$, $p_{group} = 1$, $F_{layer(4,24)} = 69.3$, $p_{layer} = 7.8 \times 10^{-13}$, $F_{group \times layer(4,24)} = 8.82$, $p_{group \times layer} = 0.00016$, two-way

repeated-measures ANOVA; control vs dnKif3A, $t_{(6)}$ = -4.09, p = 0.032 in RMS; $t_{(6)}$ = 4.05, p = 0.034 in dGCL; unpaired *t*-test; n = 4 mice each).

(**J**, **K**) Time-lapse images of control (J, red) and dnKif3A-expressing (K, red) cultured neuroblasts (green) derived from the V-SVZ of *GFP::Cent2* mice. Arrows indicate GFP::Cent2+ centrioles.

(**L**–**V**) Migration speed (L; $p = 5.3 \times 10^{-6}$, Welch's *t*-test), durations of resting (M; W = 28, $p = 3.5 \times 10^{-7}$, Mann-Whitney *U*-test) and migratory phases (N; p = 0.002, Welch's *t*-test), leading process (LP) extension speed (O), maximum LP length (P), basal body (BB) speed (Q; W = 6,669.5, $p = 6.82 \times 10^{-6}$, Mann-Whitney *U*-test), BB stride (R), frequency of backward BB migration (S; W = 73, $p = 3.17 \times 10^{-5}$, Mann-Whitney *U*-test), somal speed (T; p = 0.00012, Welch's *t*-test), somal stride (U), and frequency of polarity reversal (V; W = 93, $p = 2.9 \times 10^{-5}$, Mann-Whitney *U*-test) in control and dnKif3A-expressing cultured V-SVZ-derived neuroblasts (L-V; control, n = 21 cells; dnKif3A, n = 24 cells; five independent cultures prepared on different days).

Scale bars: 5 μm (A, B, J, K). *p < 0.05, **p < 0.01, ***p < 0.005 (adjusted with Bonferroni correction in E, H, I). Error bars indicate mean ± SEM.

Figure 4. *In vivo* identification of the primary cilium in migrating neuroblasts in the adult RMS.

(**A**–**E'**) Transmission electron microscopic (TEM) images of centrioles (A), ciliary vesicles (B, pink arrows), a procilium (C, magenta arrow), a non-extended primary cilium (D, magenta arrow), and an extended primary cilium (E, magenta arrow) in neuroblasts in the adult RMS. Green filled arrowheads indicate centrioles (A) or mother centrioles (B–E). Green open arrowheads indicate daughter centrioles (D). Boxed areas in (D) and (E) are enlarged in (D') and (E'), respectively. Blue and white arrows (D', E') indicate ciliary pockets and the ciliary axoneme, respectively. The tip of the non-extended primary cilium appeared to have access to the extracellular environment (D', yellow arrows).

(**F**, **F'**) Sequential coronal TEM images of the primary cilium in neuroblasts in the adult RMS. Coronal images of the basal body (z = 1), transition zone (z = 2–5), and doublet zone (z = 6–11) of the primary cilium are shown. The primary cilium shows 9+0 axoneme structure (F, z = 6; F', red).

Scale bars: 200 nm.

Figure 5. Ultrastructural features of V-SVZ-derived neuroblasts during proliferation and saltatory movement analyzed by SBF-SEM.

(**A**) Representative SBF-SEM images of migratory neuroblasts in the adult RMS. The migratory neuroblast consists of the growth cone, distal/proximal part of the leading process (LP), soma, and trailing process (blue). Migratory neuroblasts are tightly attached with their neighbors (all the neighbors are shown in red colors). Between neuroblasts, extracellular spaces were also observed.

(**B**–**D'**) Representative SBF-SEM images of astrocytes (B–B''), oligodendrocytes (C, C'), and microglia (D, D') in the adult RMS. Astrocytes showed long endoplasmic reticulum (B', black arrows) and intermediate filaments (B'', white arrows), and were tightly attached to a blood vessel (B, B'). Oligodendrocytes showed a round cell contour with short and dilated endoplasmic reticulum (C', back arrows), and direct contacts to myelinated and non-myelinated axons (C). Microglia showed an irregular cell contour with long processes, dark cytosol with long endoplasmic reticulum (D', black arrows) and a lysosome (D', asterisk), and extracellular spaces (D', white arrowheads).

(**E**) Time-lapse images for chain migration of DsRed-expressing cultured neuroblasts. Black and white arrowheads indicate spread and collapsed growth cones, respectively. Collapsed growth cones were only observed during somal translocation. Neuroblasts in the LP extension phase showed a spread growth cone with no swelling in their leading process (0, 5 min). Neuroblasts in the swelling-formation phase showed a spread growth cone with swelling in their leading process (7, 9 min). Neuroblasts in the somal translocation phase showed a collapsed growth cone with swelling in their leading process (12 min). Arrows indicate swelling.

(**F**–**H**) Representative three-dimensional constructions of migratory neuroblasts (blue) under LP extension phase (F), swelling-formation phase (G), and somal translocation phase (H). All the mitochondria and Golgi apparatus are shown in magenta and orange, respectively; nuclei are shown in yellow. Interactive 3D models of neuroblasts in (F–H) (without the Golgi apparatus) are shown at https://sketchfab.com/3d-models/399a425539e44087a9ba4a5c3dc5f361 (F), https://sketchfab.com/3d-models/fbaa32c3b1b34fdb9af1569cb3973475 (G), and https://sketchfab.com/3d-models/ee40d9f934e840d18ba61a653fa2f7fc (H).

(**I**–**K**) Distribution and morphology of mitochondria in migrating neuroblasts. The number of mitochondria in LP extension phase, swelling-formation phase and somal translocation phase (I; soma, $F_{(2,42)} = 6.44$, $p = 0.0036$, one-way ANOVA; LP extension phase vs swelling-formation phase, $p = 0.0032$, LP extension phase vs somal translocation phase, $p = 0.048$, Tukey-Kramer test, proximal leading process, $F_{(2,42)} = 7.89$, $p = 0.0012$, one-way ANOVA; LP extension phase vs swelling-formation phase, $p = 0.0035$, LP extension phase vs somal translocation phase, $p = 0.004$, Tukey-Kramer test, growth cone, $x^2_{(2)} = 19.2$, $p = 6.9 \times 10^{-5}$, Kruskal-Wallis test; LP extension phase vs somal translocation phase, $t(\infty) = 4.19$, $p = 8.3 \times 10^{-5}$, swelling-formation phase vs somal translocation phase, $t(\infty) = 2.88$, $p = 1.1 \times 10^{-2}$; Steel-Dwass test; n = 3 mice). Proximal leading process contains swelling in swelling-formation phase and somal translocation phase (I). Most of the mitochondria in the proximal leading process are located in the swelling in swelling-formation phase (I, 94.3 ± 1.6%) and somal translocation phase (I, 96.9 ± 1.5%). Images in (J, K) are magnified views of boxed areas in (G).

(**L**–**O**) Arl13b expression in proliferating and non-proliferating Dcx+ cells in the adult RMS. Representative images of RMS sections of adult *GFP::Cent2* mice stained for GFP (green, dot-like structures), pHH3 (L) or Ki67 (M, N) (green, nucleus), Arl13b (white), and Dcx (red). Arrows and arrowheads indicate the Arl13b+ primary cilium and centrioles, respectively (L–N). Proportions of Arl13b+ primary cilium-bearing neuroblasts in proliferating and non-proliferating Dcx+ neuroblasts are shown in (O, left) ($F_{(3,8)}$=23.15 p=0.00027 one-way ANOVA; proliferating in M phase (pHH3+) vs proliferating in G1/S/G2 phases, p=0.047, proliferating in M phase (pHH3+) vs non-proliferating, p=0.00086, proliferating in M phase (Ki67+) vs proliferating in G1/S/G2 phases, p=0.012, proliferating in M phase (Ki67+) vs non-proliferating, p=0.00031, proliferating in G1/S/G2 phases vs non-proliferating, p=0.047, Tukey-Kramer test; n=3 mice). Arl13b+ ciliary length in proliferating and non-proliferating neuroblasts is shown in (O, right) (proliferating neuroblasts, 342.1 ± 25.8 nm, n = 42 cells from three mice; non-proliferating neuroblasts, 737.4 ± 40.3 μm, n = 90 cells from three mice; W = 3,365.5, $p = 5.7 \times 10^{-13}$, Mann-Whitney *U*-test). Illustrations of the Arl13b+ primary cilium (pink, black arrows) in proliferating (green nuclei) and non-proliferating (white nucleus) Dcx+ cells are shown at the bottom of (L–N). Pairs of green dots are pairs of centrioles.

(**P**, **P’**) SBF-SEM images of dividing neuroblasts in the adult RMS. Black and green arrowheads indicate a disrupted nuclear membrane and a centriole without a primary cilium, respectively. The boxed area in (P) is enlarged in (P’).
(**Q**) Three-dimensional construction of dividing neuroblasts in the adult RMS. Mitochondria, Golgi apparatus, and centrioles are shown in magenta, orange, and green, respectively; divided nuclei are shown in yellow. An interactive 3D model of dividing neuroblasts (without the Golgi apparatus) is shown at https://sketchfab.com/3d-models/528050289d9143caab1c2b35c7fa1b3c. Raw SBF-SEM images in the adult RMS are shown in Movie 2. Scale bars: 1 μm (A–D, P), 5 μm (E), 2 μm (F–H, L–N, Q). Error bars indicate mean ± SEM. *$p < 0.05$, ***$p < 0.005$.

Figure 6. Three-dimensional ultrastructural analysis of the primary cilium in migrating neuroblasts in the adult RMS by SBF-SEM.

(**A**–**J'**) Sequential SBF-SEM images and three-dimensional constructions of centrioles (A–B'), a ciliary vesicle (C–D', pink arrows), a procilium (E–F', magenta arrows), a non-extended primary cilium (G–H', magenta arrows), and an extended primary cilium (I–J', magenta arrows). Green filled arrowheads indicate centrioles (A) or mother centrioles (C, E, G, I). Green open arrowheads indicate daughter centrioles (C, G, I). Pink arrows in (D', F', H', J') indicate primary cilium orientation in the cells.

(**K**, **K'**) Three-dimensional construction of an extended primary cilium (K') in an FLP-bearing neuroblast in the adult OB. The arrow indicates an FLP.

Interactive 3D models of neuroblasts in (B, D, F, H, J, K) are shown at https://sketchfab.com/3d-models/62e9a69dec414b31a64e8d0158bf7945 (B), https://sketchfab.com/3d-models/1c9eb432686748e8ac537afab59e335a (D), https://sketchfab.com/3d-models/5a5ba2836417475a9bb7513056824055 (F), https://sketchfab.com/3d-models/73abab8f28364a3c99277f7086c19c85 (H), https://sketchfab.com/3d-models/46cff34b6a9947bfa95fbdd12b0696f4 (J), and https://sketchfab.com/3d-models/0e3963794ca74fc2a15d8cdde4e3c0ee.

Scale bars: 200 nm (A, C, E, G, I), 5 μm (B, D, F, H, J, K).

Figure 7. Changes in subcellular localization, length, and orientation of the primary cilium during saltatory movement of migrating neuroblasts in the adult RMS.

(**A**) The proportions of immature migratory neuroblasts that have centrioles, a ciliary vesicle, a procilium, a non-extended primary cilium, and an extended primary cilium in the adult RMS ($F_{(4,20)}$ = 56.59, p = 1.3 × 10^{-10}, one-way ANOVA; centrioles vs non-extended primary cilium, p<0.0000001, ciliary vesicle vs non-extended primary cilium, p < 0.0000001, procilium vs non-extended primary cilium, p < 0.0000001, extended primary cilium vs non-extended primary cilium, p<0.0000001, Tukey-Kramer test; n = 5 mice) and OB ($F_{(4,10)}$ = 17.28, p = 0.00017, one-way ANOVA; centrioles vs extended primary cilium, p = 0.00034, ciliary vesicle vs extended primary cilium, p = 0.0005, procilium vs extended primary cilium, p = 0.00034, non-extended primary cilium vs extended primary cilium, p = 0.012, Tukey-Kramer test; n = 3 mice).

(**B**) The proportions of neuroblasts that have centrioles, a ciliary vesicle, a procilium, a non-extended primary cilium, and an extended primary cilium during leading-process (LP) extension phase, the swelling-formation phase, and somal translocation phase in the adult RMS ($F_{phase(2,12)}$ = - 0.004, p_{phase} = 1, $F_{\text{class }(4,48)}$ = 75.52, p_{class} < 2.2 × 10^{-16}, $F_{\text{phase x class}(8,48)}$ = 9.69, $p_{\text{phase x class}}$ = 7.1 × 10^{-8}, two-way repeated-measures ANOVA; $F_{(2,12)}$ = 20.31, p = 0.00014, one-way ANOVA; LP extension phase vs swelling-formation phase, p = 0.00092, somal translocation phase vs swelling-formation phase, p = 0.0045, in procilium; $F_{(2,12)}$ = 13.02, p = 0.00099, one-way ANOVA; LP extension phase vs swelling-formation phase, p = 0.0071, somal translocation phase vs swelling-formation phase, p = 0.02, in non-extended primary cilium; $F_{(2,12)}$ = 18.55, p = 0.00021, one-way ANOVA; LP extension phase vs swelling-formation phase, p = 0.00088, somal translocation phase vs swelling-formation phase, p = 0.023, in extended primary cilium; Tukey-Kramer test; n = 5 mice). *p < 0.05, **p < 0.01, ***p < 0.005 (adjusted with Bonferroni correction).

(**C**) Length of the non-extended and extended primary cilium in immature neuroblasts in the adult RMS and OB (RMS vs OB, W = 869.5 p = 0.012, in non-extended primary cilium; Mann-Whitney U-test; $t_{(48)}$ = 6.68, p = 2.3 × 10^{-8}, in extended primary cilium; non-extended primary cilium vs extended primary cilium, $t_{(19)}$ = -2.7, p = 0.014, in OB; unpaired t-test; n = 3 mice each).

(**D**–**K**) Sequential SBF-SEM images and three-dimensional constructions of extended primary cilium contacting a neighboring neuroblast (D–E, red), astrocyte (F–G, green), granule cell (H–I, orange), and presynaptic structure (J–K, yellow). White arrows and arrowheads indicate postsynaptic density and synaptic vesicles, respectively (J').

(**L**) EB3::GFP speed in the growth cone, distal/proximal leading process, and soma during saltatory movement of cultured chain-forming migrating neuroblasts ($x^2_{(3)}$ = 14.67, p = 0.0021, Kruskal-Wallis test; distal leading process vs soma, $t(\infty)$ = 3.66, p = 0.0014, in LP extension phase; $x^2_{(3)}$ = 17.77, p=0.00049, Kruskal-Wallis test; distal leading process vs soma, $t(\infty)$ = 3.13, p=0.0094, growth cone vs proximal leading process, $t(\infty)$ = 2.84, p = 0.023, proximal leading process vs soma, $t(\infty)$ = 3.12, p = 0.0097, in swelling-formation phase; $x^2_{(3)}$ = 53.72, p=1.3 × 10^{-11}, Kruskal-Wallis test; distal leading process vs soma, $t(\infty)$ = 6.87, p = 4.0 × 10^{-11}, growth cone vs soma, $t(\infty)$ = 4.19, p = 1.6 × 10^{-4}, proximal leading process vs soma, $t(\infty)$ = 3.45 p = 3.1 × 10^{-3}, in somal translocation phase; $x^2_{(2)}$ = 8.61, p=0.0014, Kruskal-Wallis test; LP extension phase vs somal translocation phase, $t(\infty)$ = 2.71, p = 0.0018, swelling-formation phase vs somal translocation phase, $t(\infty)$ = 2.4, p = 0.043, in growth cone; $x^2_{(2)}$ = 7.21, p < 2.2 × 10^{-16}, Kruskal-Wallis test; LP extension phase vs somal translocation phase, $t(\infty)$ = 7.46, p = 2.7 × 10^{-13}, swelling-formation phase vs somal translocation phase, $t(\infty)$ = 6.55, p = 1.8 × 10^{-10}, in distal leading process; $x^2_{(2)}$ = 8.8, p = 0.0012, Kruskal-Wallis test; LP extension phase vs swelling-formation phase, $t(\infty)$ = 2.43, p = 0.04, swelling-formation phase vs somal translocation phase, $t(\infty)$ = 2.69, p=0.019, in proximal leading process; $x^2_{(2)}$ = 22.18, p = 1.5 × 10^{-5}, Kruskal-Wallis test; LP extension phase vs somal translocation phase, $t(\infty)$ = 4.1, p = 0.00012, swelling-formation phase vs somal translocation phase, $t(\infty)$ = 4.11, p = 0.00012, in soma; Steel-Dwass test). *p < 0.05, **p < 0.01, ***p < 0.005, #p < 0.05 (vs LP extension phase and swelling-formation phase in growth cone), §§§p < 0.005 (vs LP extension phase and swelling-formation phase in distal leading process), ‡p < 0.05 (vs LP extension phase and somal translocation phase in proximal leading process), †††p < 0.005 (vs LP extension phase and swelling-formation phase in soma). Parentheses indicate the number of events from eight cells in three independent cultures.

(**M**) The proportions of immature and mature primary cilium that orient posteriorly under LP extension phase, the swelling-formation phase, and somal translocation

phase in the adult RMS (p = 0.00015, Fisher's exact test, somal translocation phase vs swelling-formation phase, p = 0.0064, LP extension phase vs somal translocation phase, p = 0.00098, in ciliary vesicle; p = 0.00015, Fisher's exact test; somal translocation phase vs swelling-formation phase, p = 0.0078, LP extension phase vs somal translocation phase, p = 0.00075, in procilium; $p = 6.2 \times 10^{-8}$, Fisher's exact test, somal translocation phase vs swelling-formation phase, p = 0.00012, LP extension phase vs somal translocation phase, $p = 9.4 \times 10^{-7}$, in non-extended primary cilium; $p = 9.5 \times 10^{-5}$, Fisher's exact test, somal translocation phase vs swelling-formation phase, p = 0.00039, LP extension phase vs somal translocation phase, p = 0.014, in extended primary cilium; n = 5 mice). *p < 0.05, ***p < 0.005 (vs LP extension phase); §p < 0.05, §§§p < 0.005 (vs swelling-formation phase).

Error bars indicate mean ± SEM. Scale bars: 1 μm.

Figure 8. Spatiotemporal regulation of the primary cilium in V-SVZ-derived migrating neuroblasts in the postnatal brain.

(**A**) The primary cilium in proliferating neuroblasts in the postnatal RMS. Ciliogenesis is suppressed during mitosis (green nuclei) of V-SVZ-derived migrating neuroblasts in the RMS.

(**B**) The primary cilium in migration of chain-forming neuroblasts in the RMS. The primary cilium (pink) is submerged in the cytosol and orients posteriorly during leading process extension, when a spread growth cone is observed. During the swelling-formation phase, the primary cilium is extended from the cell surface and moves forward within the swelling. The primary cilium is not extended when neuroblasts translocate their soma. The orientation of the primary cilium is related to active MT polymerization (bold blue arrows) in migration phases.

(**C**) The primary cilium in migration of FLP-bearing neuroblasts in the postnatal OB. The FLP is transiently formed from the proximal part of the leading process prior to somal translocation (Sawada et al., 2018). FLP formation coincides with active and local MT reorganization in the proximal leading process (bold blue arrows), which maintains migration termination in neuroblasts. The elongation and extension of the primary cilium are promoted in individual decelerating neuroblasts in the OB.

Table 1. Numbers of neuroblasts examined in the SBF-SEM analyses.

The numbers of analyzed neuroblasts in the SBF-SEM analyses are shown. Parentheses indicate the numbers of neuroblasts with partial cell morphology (partial cells).

Movie 1. Time-lapse imaging of control (red) and dnKif3A-expressing (red) neuroblasts (green) derived from the V-SVZ of *GFP::Cent2* mice.

Movie 2. Sequential SBF-SEM images in the adult RMS.
Representative sequential SBF-SEM images (1,156 sections) in the adult RMS are shown. Neuroblasts shown in Figure 5F, 5G, and 5H appear in yellow, red, and blue, respectively. Dividing neuroblasts shown in Figure 5Q appear in green.

Movie 3. Three-dimensional reconstruction of a migratory neuroblast in the adult RMS.
Blue indicates the cell contour of the migratory neuroblast. Green, yellow, orange, and magenta indicate centrioles, nucleus, the Golgi apparatus, and mitochondria, respectively.

Movie 4. Three-dimensional reconstruction image of a migratory neuroblast during leading process extension.
Green, yellow, orange, and magenta indicate centrioles, nucleus, Golgi apparatus, and mitochondria, respectively.

Movie 5. Three-dimensional reconstruction image of a migratory neuroblast in the swelling-formation phase.
Green, yellow, orange, and magenta indicate centrioles, nucleus, Golgi apparatus, and mitochondria, respectively.

Movie 6. Three-dimensional reconstruction image of a migratory neuroblast during somal translocation.
Green, yellow, orange, and magenta indicate centrioles, nucleus, Golgi apparatus, and mitochondria, respectively.

Movie 7. Three-dimensional reconstruction image of dividing neuroblasts.
Blue and yellow indicate the cell contour and divided nuclei, respectively. Green, orange, and magenta indicate centrioles, Golgi apparatus, and mitochondria, respectively.

Movie 8. Three-dimensional reconstruction image of a neuroblast having centrioles.

Blue and green indicate the cell contour and centrioles, respectively.

Movie 9. Three-dimensional reconstruction image of a neuroblast having a ciliary vesicle.

Blue, green, and magenta indicate the cell contour, centrioles, and the ciliary vesicle, respectively.

Movie 10. Three-dimensional reconstruction image of a neuroblast having a procilium.

Blue, green, and magenta indicate the cell contour, centrioles, and the ciliary membrane, respectively.

Movie 11. Three-dimensional reconstruction image of a neuroblast having a non-extended primary cilium.

Blue, green, and magenta indicate the cell contour, centrioles, and the ciliary membrane, respectively.

Movie 12. Three-dimensional reconstruction image of a neuroblast having an extended primary cilium.

Blue, green, and magenta indicate the cell contour, centrioles, and the ciliary membrane, respectively.

Movie 13. Time-lapse imaging of EB3::GFP and dTomato::Cent2 during saltatory movement of a cultured V-SVZ-derived migrating neuroblast.

The migratory behavior of an EB3::GFP- (white) and dTomato::Cent2 (magenta)-expressing V-SVZ-derived neuroblast was recorded at 4-s intervals by superresolution microscopy. Leading-process extension phase, 0–440 s swelling-formation phase, 444–1,280 s; somal translocation phase, 1,284–1,920 s. Scale bar: 2 μm.

Data		Ciliary types					Total
		Centrioles	Ciliary vesicle	Procilium	Non-extended primary cilium	Extended primary cilium	
Results	Neuroblast orientation	-	-	-	-	-	418 (88)
Fig. 5F-H (Fig. 7B, M)	Leading-process extension phase	22 (0)	23 (0)	10 (0)	82 (0)	6 (0)	143 (0)
	Swelling-formation phase	10 (0)	14 (0)	28 (0)	33 (0)	22 (0)	107 (0)
	Somal translocation phase	9 (0)	11 (0)	8 (0)	44 (0)	8 (0)	80 (0)
Fig. 5I	Leading-process extension phase	-	-	-	-	-	15 (0)
	Swelling-formation phase	-	-	-	-	-	15 (0)
	Somal translocation phase	-	-	-	-	-	15 (0)
Results	Mitochondrial length	-	-	-	-	-	18 (0)
Fig. 5Q	Mitosis	-	-	-	-	-	1 (0)
Fig. 7A	RMS	41 (0)	48 (0)	46 (0)	159 (0)	36 (0)	330 (0)
	OB	1 (1)	2 (2)	1 (1)	7 (7)	14 (14)	25 (25)
Fig. 7C	RMS	-	-	-	159 (0)	36 (0)	195 (0)
	OB	-	-	-	7 (7)	14 (14)	21 (21)
Fig. 7D, E	Neuroblast	-	-	-	-	28 (0)	28 (0)
Fig. 7F, G	Astrocyte	-	-	-	-	8 (0)	8 (0)
Fig. 7H, I	Granule cell	-	-	-	-	3 (3)	3 (3)
Fig. 7J, K	Presynaptic structure	-	-	-	-	11 (11)	11 (11)

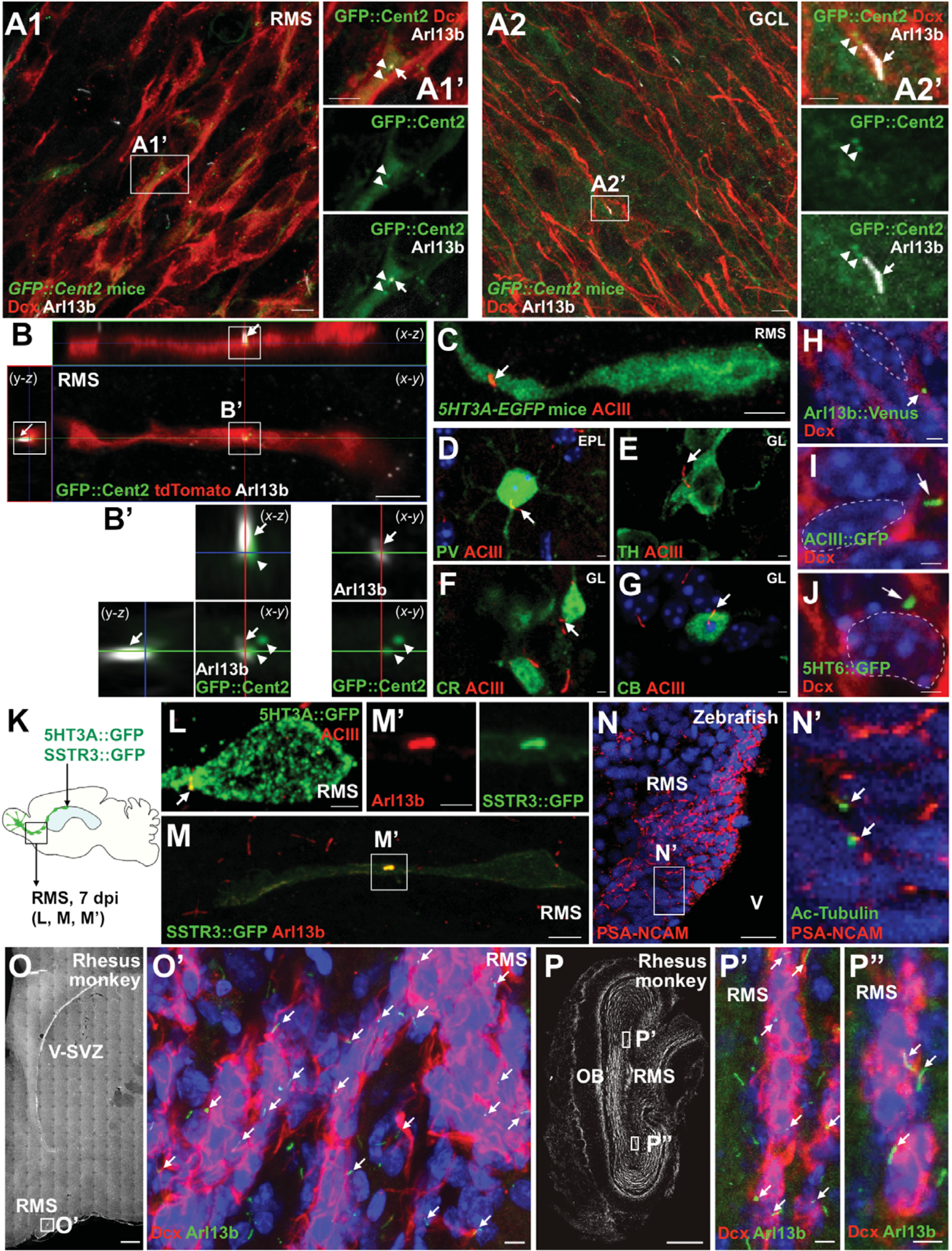
A1
RMS
A1'
GFP::Cent2 Dcx
Arl13b
A1'
GFP::Cent2
GFP::Cent2
Arl13b
GFP::Cent2 mice
Dcx Arl13b
A2
GCL
A2'
GFP::Cent2 Dcx
Arl13b
A2'
GFP::Cent2
GFP::Cent2
Arl13b
GFP::Cent2 mice
Dcx Arl13b
B
(x-z)
(y-z)
RMS
(x-y)
B'
GFP::Cent2 tdTomato Arl13b
B'
(x-z)
(x-y)
Arl13b
(y-z)
(x-y)
Arl13b
GFP::Cent2
(x-y)
GFP::Cent2
C
RMS
5HT3A-EGFP mice ACIII
D
EPL
PV ACIII
E
GL
TH ACIII
F
GL
CR ACIII
G
GL
CB ACIII
H
Arl13b::Venus
Dcx
I
ACIII::GFP
Dcx
J
5HT6::GFP
Dcx
K
5HT3A::GFP
SSTR3::GFP
RMS, 7 dpi
(L, M, M')
L
5HT3A::GFP
ACIII
RMS
M'
Arl13b
SSTR3::GFP
M
M'
RMS
SSTR3::GFP Arl13b
N
Zebrafish
RMS
N'
V
PSA-NCAM
N'
Ac-Tubulin
PSA-NCAM
O
Rhesus
monkey
V-SVZ
RMS
O'
O'
RMS
Dcx Arl13b
P
Rhesus
monkey
P'
OB
RMS
P''
P'
RMS
Dcx Arl13b
P''
RMS
Dcx Arl13b

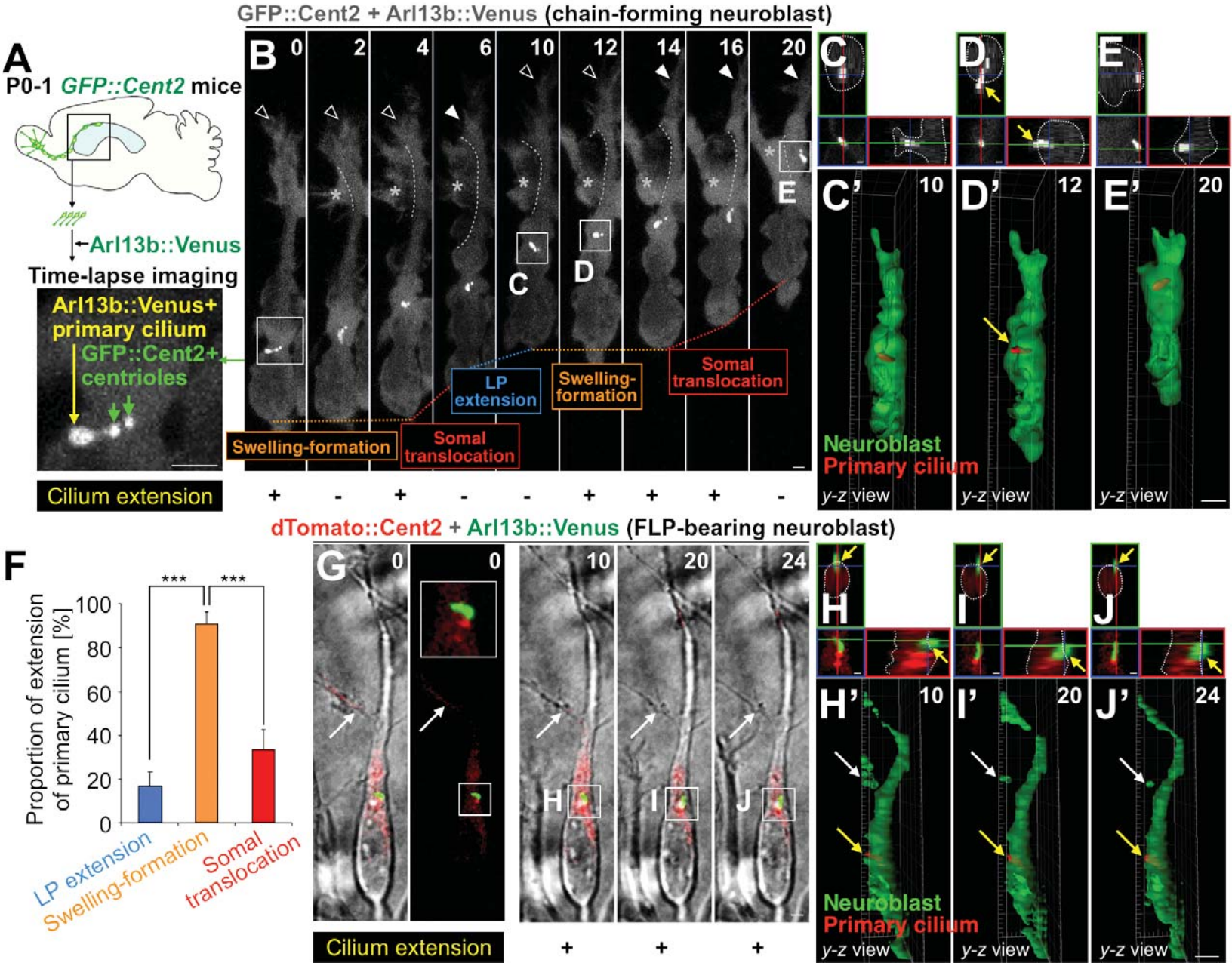
GFP::Cent2 + Arl13b::Venus (chain-forming neuroblast)
A
P0-1 GFP::Cent2 mice
Arl13b::Venus
Time-lapse imaging
Arl13b::Venus+ primary cilium
GFP::Cent2+ centrioles
B
0
2
4
6
10
12
14
16
20
C
D
E
LP extension
Swelling-formation
Somal translocation
Swelling-formation
Somal translocation
Cilium extension
+ - + - - + + + -
C'
10
D'
12
E'
20
Neuroblast
Primary cilium
y-z view
y-z view
y-z view
dTomato::Cent2 + Arl13b::Venus (FLP-bearing neuroblast)
F
Proportion of extension of primary cilium [%]
100
80
60
40
20
0
***
***
LP extension
Swelling-formation
Somal translocation
G
0
0
10
20
24
H
I
J
Cilium extension
+ + +
H'
10
I'
20
J'
24
Neuroblast
Primary cilium
y-z view
y-z view
y-z view

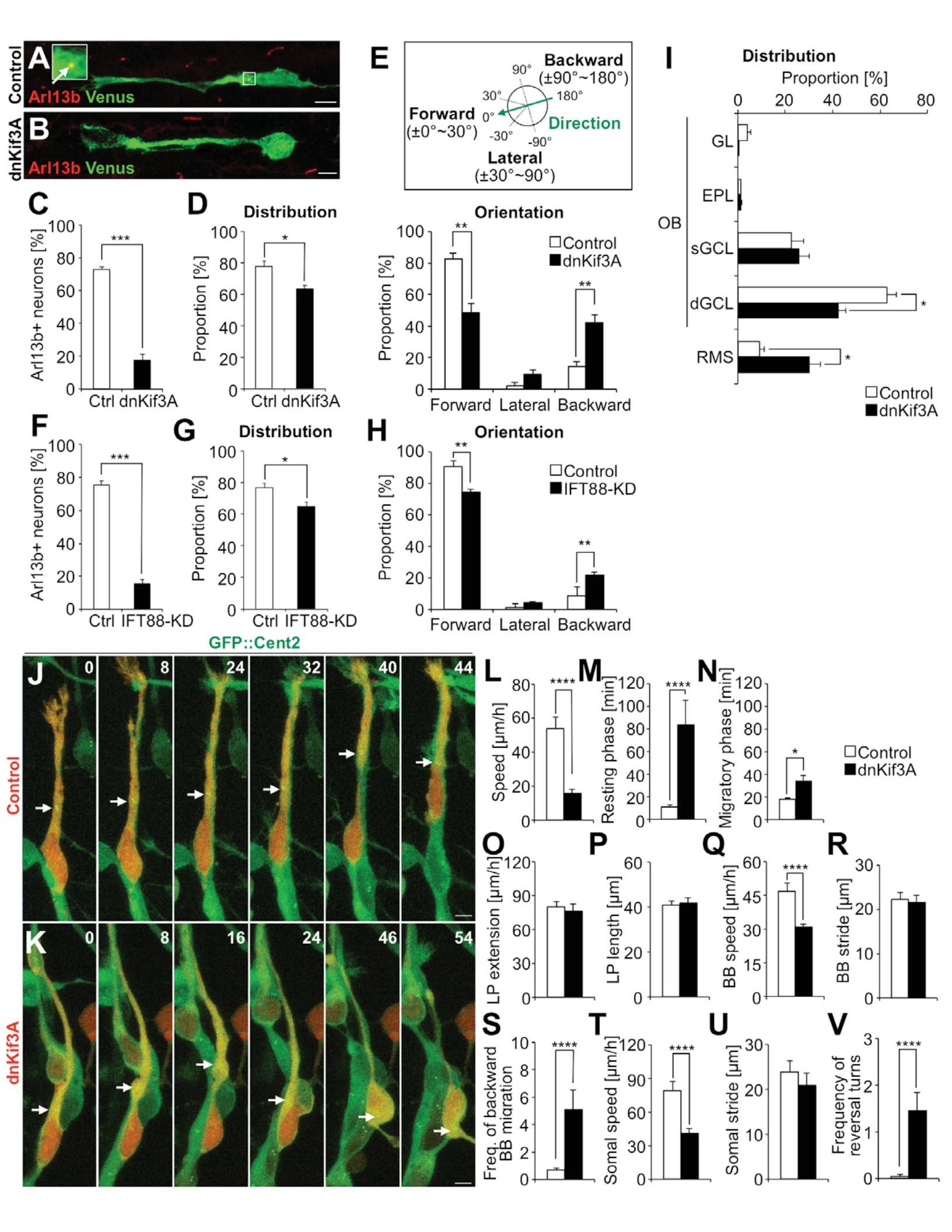
A
Control
Arl13b Venus
B
dnKif3A
Arl13b Venus
C
Arl13b+ neurons [%]
Ctrl dnKif3A
D
Distribution
Proportion [%]
Ctrl dnKif3A
E
Backward
(±90°~180°)
Forward
(±0°~30°)
Lateral
(±30°~90°)
Direction
Orientation
Proportion [%]
Control
dnKif3A
Forward Lateral Backward
I
Distribution
Proportion [%]
OB
GL
EPL
sGCL
dGCL
RMS
Control
dnKif3A
F
Arl13b+ neurons [%]
Ctrl IFT88-KD
G
Distribution
Proportion [%]
Ctrl IFT88-KD
H
Orientation
Proportion [%]
Control
IFT88-KD
Forward Lateral Backward
GFP::Cent2
J
Control
K
dnKif3A
L
Speed [μm/h]
M
Resting phase [min]
N
Migratory phase [min]
Control
dnKif3A
O
LP extension [μm/h]
P
LP length [μm]
Q
BB speed [μm/h]
R
BB stride [μm]
S
Freq. of backward BB migration
T
Somal speed [μm/h]
U
Somal stride [μm]
V
Frequency of reversal turns

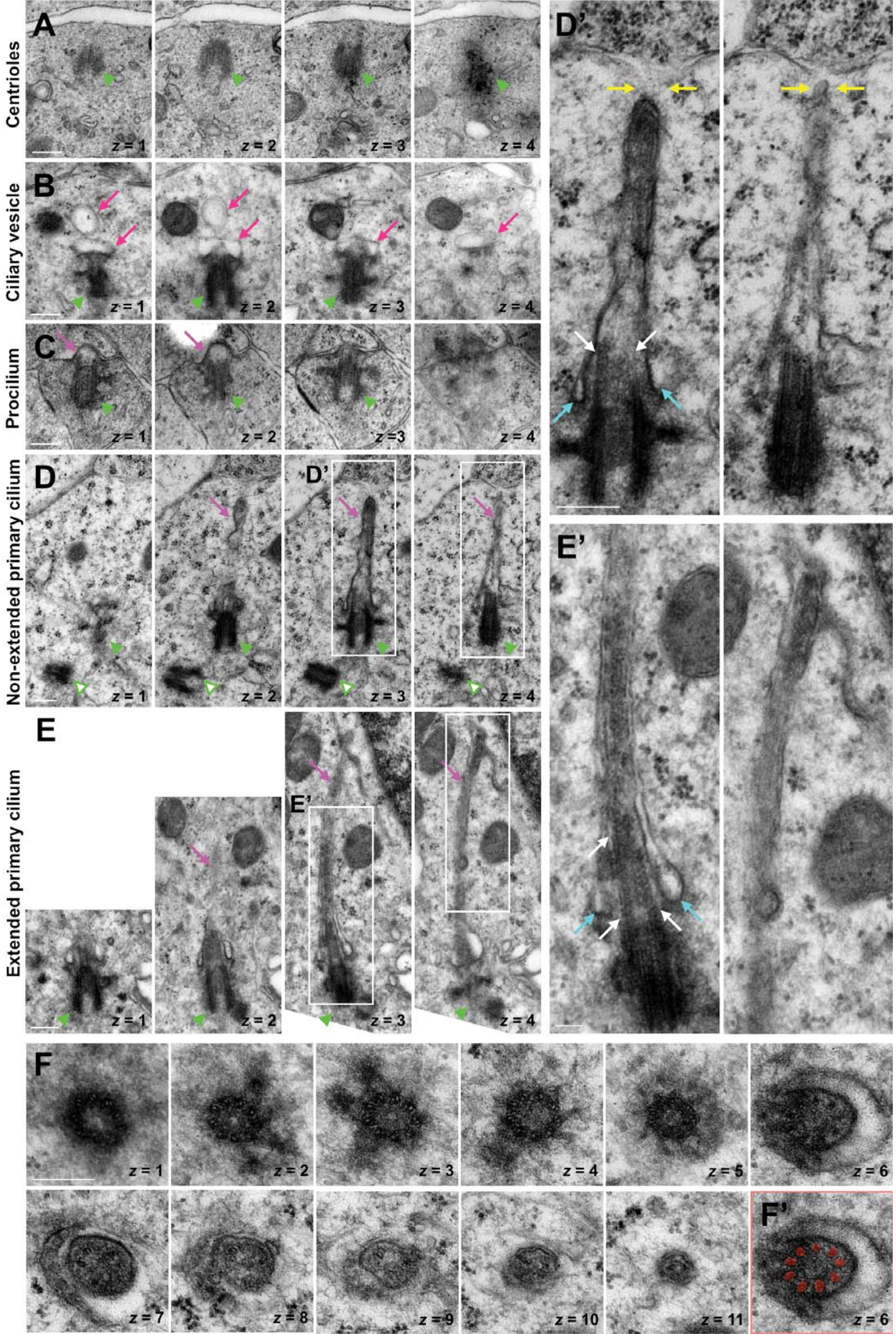
Centrioles
A
z = 1
z = 2
z = 3
z = 4
Ciliary vesicle
B
z = 1
z = 2
z = 3
z = 4
Procilium
C
z = 1
z = 2
z =3
z = 4
Non-extended primary cilium
D
D'
z = 1
z = 2
z = 3
z = 4
D'
E
E'
Extended primary cilium
z = 1
z = 2
E'
z = 3
z = 4
E'
F
z = 1
z = 2
z = 3
z = 4
z = 5
z = 6
z = 7
z = 8
z = 9
z = 10
z = 11
F'
z = 6

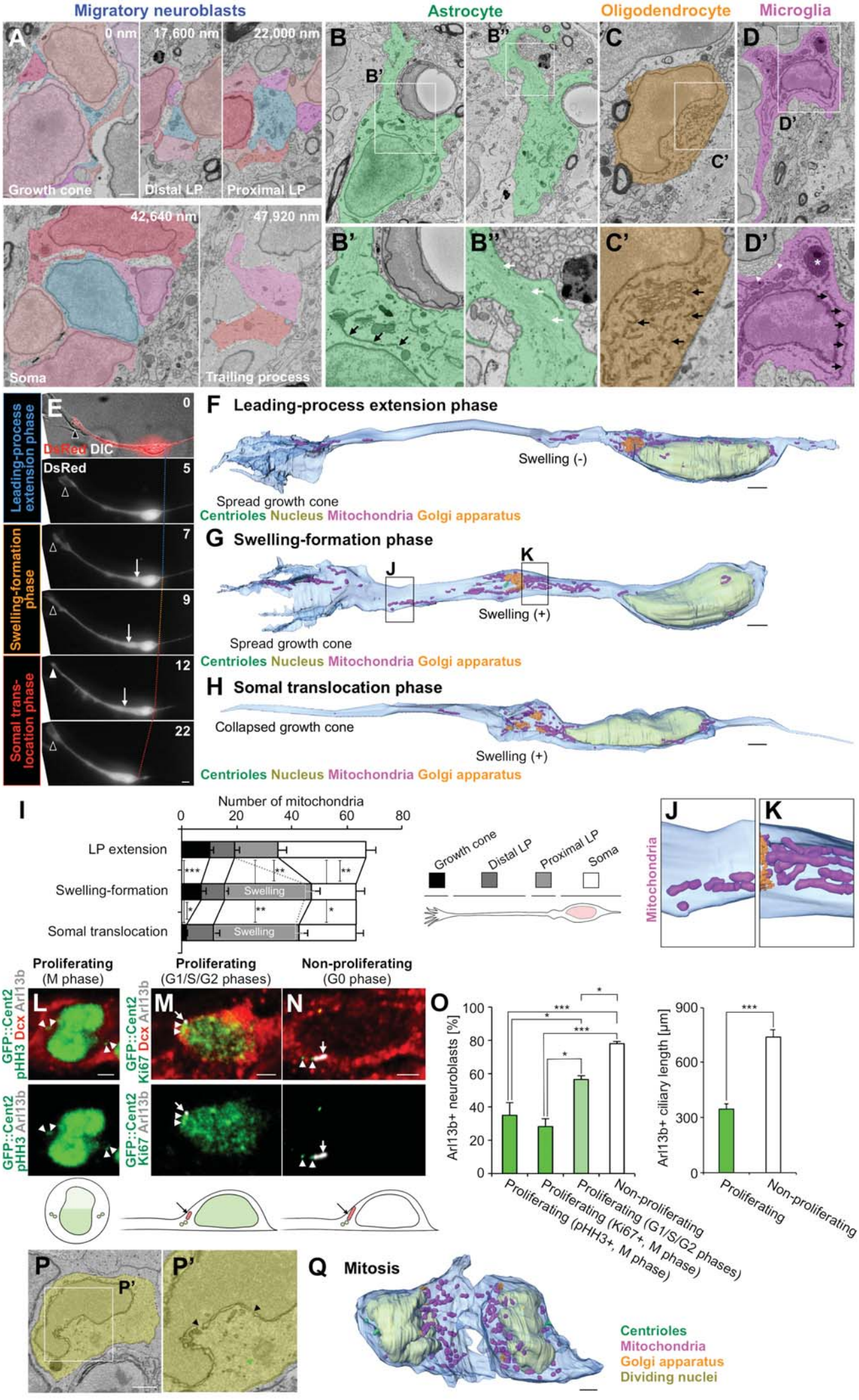
Migratory neuroblasts
Astrocyte
Oligodendrocyte
Microglia
A
0 nm
17,600 nm
22,000 nm
Growth cone
Distal LP
Proximal LP
42,640 nm
47,920 nm
Soma
Trailing process
B
B'
B''
C
C'
D
D'
Leading-process extension phase
Swelling-formation phase
Somal trans-location phase
E
DsRed DIC
DsRed
0
5
7
9
12
22
F Leading-process extension phase
Swelling (-)
Spread growth cone
Centrioles Nucleus Mitochondria Golgi apparatus
G Swelling-formation phase
J
K
Swelling (+)
Spread growth cone
Centrioles Nucleus Mitochondria Golgi apparatus
H Somal translocation phase
Collapsed growth cone
Swelling (+)
Centrioles Nucleus Mitochondria Golgi apparatus
I
Number of mitochondria
0
20
40
60
80
LP extension
Swelling-formation
Somal translocation
Swelling
Growth cone
Distal LP
Proximal LP
Soma
J
K
Mitochondria
Proliferating (M phase)
Proliferating (G1/S/G2 phases)
Non-proliferating (G0 phase)
GFP::Cent2 pHH3 Dcx Arl13b
GFP::Cent2 pHH3 Arl13b
GFP::Cent2 Ki67 Dcx Arl13b
GFP::Cent2 Ki67 Arl13b
L
M
N
O
Arl13b+ neuroblasts [%]
Proliferating (pHH3+, M phase)
Proliferating (Ki67+, M phase)
Proliferating (G1/S/G2 phases)
Non-proliferating
Arl13b+ ciliary length [µm]
Proliferating
Non-proliferating
P
P'
Q Mitosis
Centrioles
Mitochondria
Golgi apparatus
Dividing nuclei

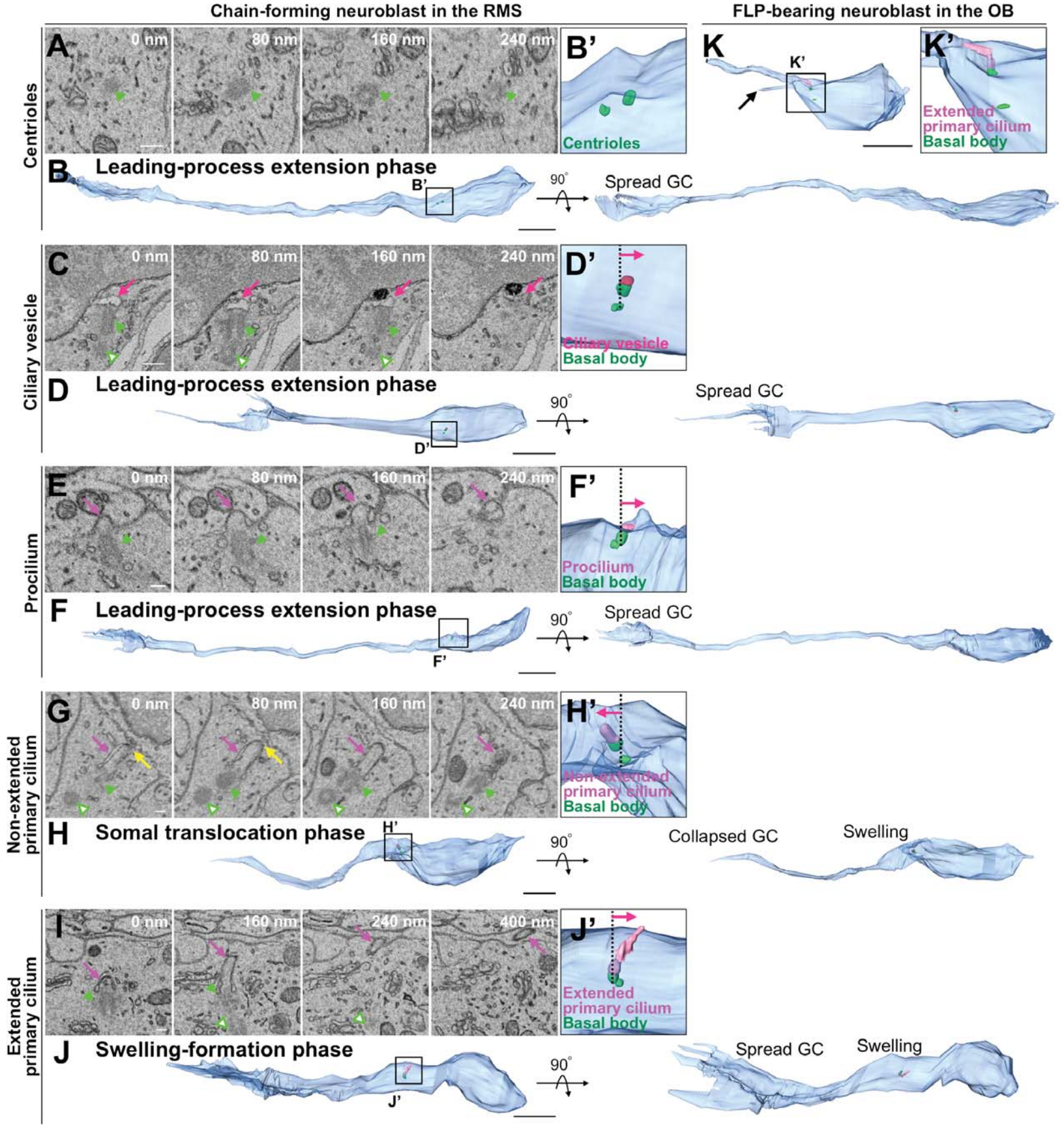
Chain-forming neuroblast in the RMS
FLP-bearing neuroblast in the OB
Centrioles
Ciliary vesicle
Procilium
Non-extended primary cilium
Extended primary cilium
A
0 nm
80 nm
160 nm
240 nm
B'
Centrioles
K
K'
Extended primary cilium
Basal body
B
Leading-process extension phase
90°
Spread GC
C
D'
Ciliary vesicle
Basal body
D
E
F'
Procilium
Basal body
F
G
H'
Non-extended primary cilium
Basal body
H
Somal translocation phase
Collapsed GC
Swelling
I
400 nm
J'
J
Swelling-formation phase

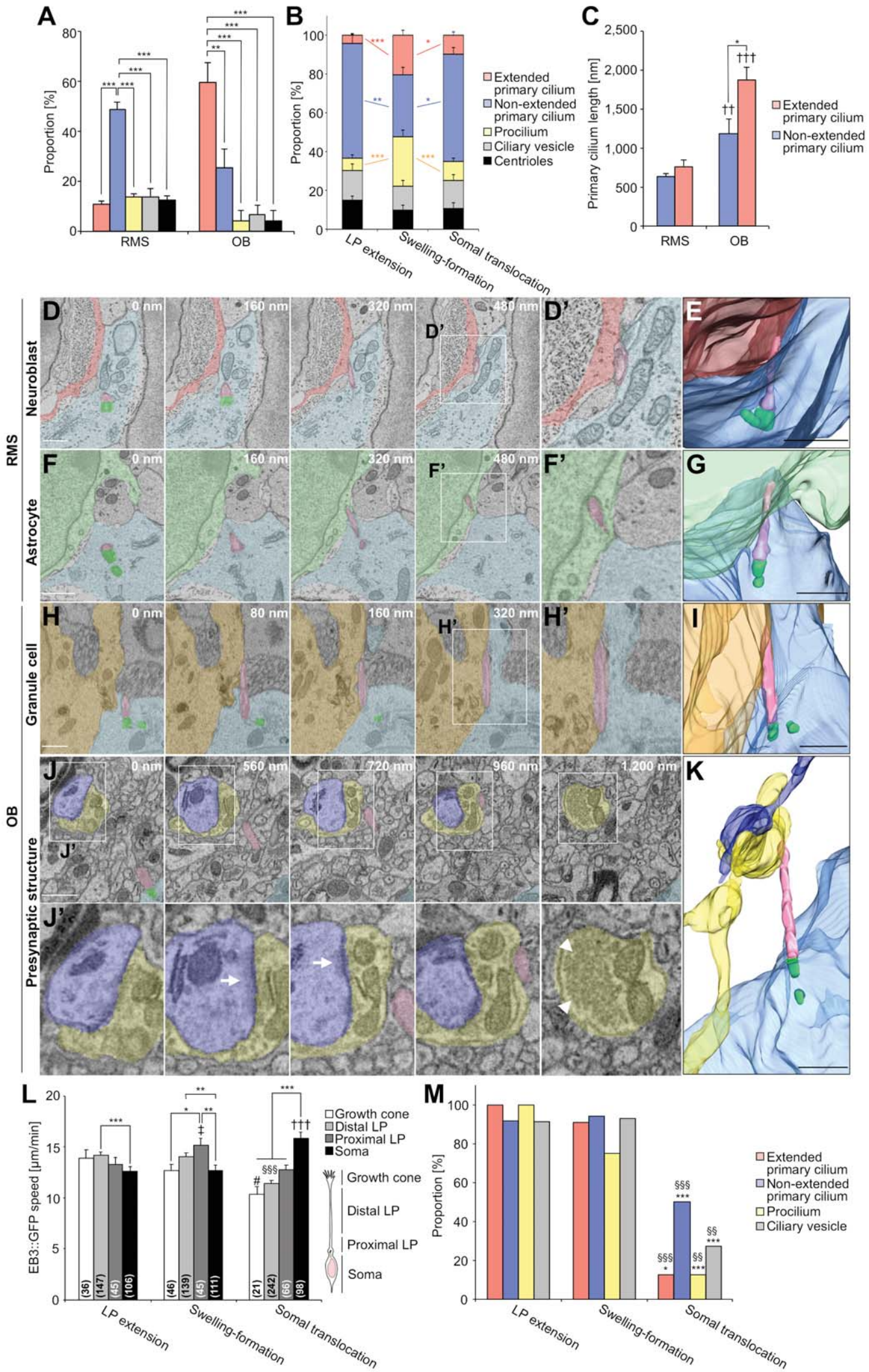
A
Proportion [%]
RMS
OB
B
Proportion [%]
LP extension
Swelling-formation
Somal translocation
Extended primary cilium
Non-extended primary cilium
Procilium
Ciliary vesicle
Centrioles
C
Primary cilium length [nm]
RMS
OB
Extended primary cilium
Non-extended primary cilium
RMS
OB
Neuroblast
Astrocyte
Granule cell
Presynaptic structure
D
D'
E
F
F'
G
H
H'
I
J
J'
K
0 nm
160 nm
320 nm
480 nm
80 nm
560 nm
720 nm
960 nm
1,200 nm
L
EB3::GFP speed [µm/min]
Growth cone
Distal LP
Proximal LP
Soma
LP extension
Swelling-formation
Somal translocation
M
Proportion [%]
Extended primary cilium
Non-extended primary cilium
Procilium
Ciliary vesicle

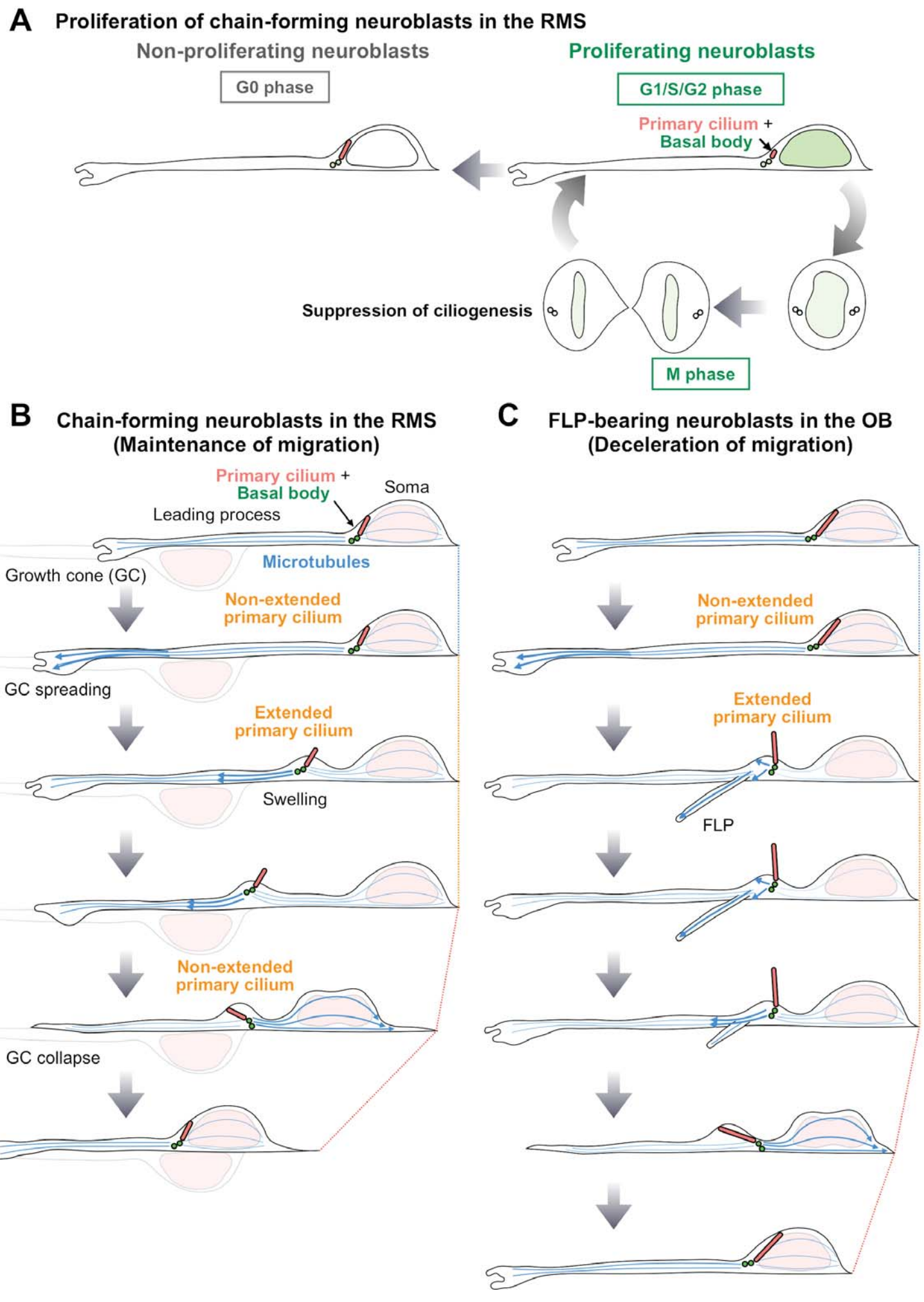
A
Proliferation of chain-forming neuroblasts in the RMS
Non-proliferating neuroblasts
Proliferating neuroblasts
G0 phase
G1/S/G2 phase
Primary cilium +
Basal body
Suppression of ciliogenesis
M phase
B
Chain-forming neuroblasts in the RMS
(Maintenance of migration)
Primary cilium +
Basal body
Soma
Leading process
Microtubules
Growth cone (GC)
Non-extended
primary cilium
GC spreading
Extended
primary cilium
Swelling
Non-extended
primary cilium
GC collapse
C
FLP-bearing neuroblasts in the OB
(Deceleration of migration)
Non-extended
primary cilium
Extended
primary cilium
FLP